國立臺灣大學（碩）博士學位論文
口試委員會審定書

尋找中性 K 介子衰變至準純量 sgoldstino 粒子

Search for K_L decay to light pseudoscalar sgoldstino at E391a

　　本論文係吳孟霖君（R94222025）在國立臺灣大學物理學系、所完成之碩（博）士學位論文，於民國九十六年十二月二十七日承下列考試委員審查通過及口試及格，特此證明

口試委員：

_____（簽名）
　　　　　（指導教授）

_____　　_____

_____

_____

MASTER'S THESIS

Search for K_L^0 decay to light pseudoscalar sgoldstino at E391a

Meng-Lin Wu

Department of Physics, National Taiwan University,
Taipei, Taiwan, R.O.C.

Advisor
Prof. Yee Hsiung
Department of Physics, National Taiwan University,
Taipei, Taiwan, R.O.C.

December 2007

K π^0

sgoldstino(X   )

E391a

90%

$Br(K_L\text{-}{>}\pi^0X(181.7\ \text{MeV})) < 2.26{\times}10^{-6}$

$Br(K_L\text{-}{>}\pi^0X(198.0\ \text{MeV})) < 1.97{\times}10^{-6}$

$Br(K_L\text{-}{>}\pi^0X(214.3\ \text{MeV})) < 1.81{\times}10^{-6}$

$Br(K_L\text{-}{>}\pi^0X(230.6\ \text{MeV})) < 1.17{\times}10^{-6}$

Abstract

With $m_X = 214.3$ MeV as hinted by a previous HyperCP experiment, we report the first search of the decay $K_L \to \pi^0 X$ using the Run2 data sample recorded with the E391a detector at KEK-PS. The particle X has a theoretical interpretation as the pseudoscalar sgoldstino. It is predicted to decay predominantly to two photons. As a result of this search, we set a 90% confidence-level upper limit for its branching ratio at $\mathcal{B}(K_L \to \pi^0 X) < 1.81 \times 10^{-6}$. We also performed a search for the same mode assuming different m_X: 181.7MeV, 198MeV, 230.6MeV and set respective 90% confidence-level upper limits: $\mathcal{B}(K_L \to \pi^0 X_{181.7}) < 2.26 \times 10^{-6}$, $\mathcal{B}(K_L \to \pi^0 X_{198.0}) < 1.97 \times 10^{-6}$ and $\mathcal{B}(K_L \to \pi^0 X_{230.6}) < 1.17 \times 10^{-6}$. The K_L flux for the E391a Run2 data set is also measured to be $(4.83 \pm 0.21) \times 10^9$ in the fiducial region.

Acknowledgments

I would like to thank my advisor Prof. Yee Hsiung. I thank him for leading my way into the field of high energy physics. Prof. Hsiung was always kind and patient in guiding my research. I could not have completed this thesis without his insights to my problems. I also gained a lot of knowledge in his courses.

I'm grateful to Prof. Min-Zu Wang for chairing the weekly group meeting, which uncovered some blindspots otherwise unknown to me. I also thank Prof. Wei-Shu Hou and Prof. Paoti Chang for their useful comments and suggestions.

I wish to thank the members of NTU HEP. I'd especially like to thank Dr. Kai-Feng Chen for his many useful comments both in and out of research, and for helping others to his fullest. I appreciate fellow student Yu-Chen Tung for his support and inspiration. I also thank students Yi-Zhe Wang, Zheng-Hao Chen, Jui-Te Wei, Kai-Yi Gao and Tai-Hsiang Ho for all the fruitful discussions.

The E391a group has offered me a great deal of assistance. I thank Prof. T. Inagaki for passing on his experiences. I also thank G.Y. Lim and T.K. Komatsubara for the wonderful analysis meetings. I'd especially want to thank Ph.D students Gabriel Perdue and Toshi Sumida. They have given me countless useful advices and invaluable knowledge of the E391a experiment. I wish the E391a collaboration the best of luck in future researches.

An able mind is not without a healthy body. Therefore, I thank Dr. Sheng-Wen Lin for inviting me to the badminton club.

Finally, I must express my deep gratitude toward my parents. They have supported my every decision in life. They have always loved me through and through. I could not have accomplished anything, let alone a research, were it not for their love. I'm forever indebted to my parents.

Meng-Lin Wu, 2007

Contents

List of Figures

List of Tables

Chapter 1

Introduction

1.1 The X particle - HyperCP experiment

The HyperCP collaboration is a fixed-target experiment at Fermilab, which searches for CP violation in charged Ξ and Λ hyperon decays, as well as for rare and forbidden hyperon and kaon decays.

In Jan 2005, HyperCP reported evidence for a very rare baryon decay $\Sigma^+ \to p + \mu^+ + \mu^-$ [1]. The 3 observed events fell in a narrow range of dimuon mass within resolution, as shown in Fig. 1.1. This may indicate that the decays proceeded via an intermediate state, $\Sigma^+ \to pP^0, P^0 \to \mu^+ + \mu^-$ with a P^0 mass of $214.3 \pm 0.5 \text{MeV}/c^2$ and branching ratio $\mathcal{B}(\Sigma^+ \to pP^0, P^0 \to \mu^+\mu^-) = [3.1^{+2.4}_{-1.9} \pm 1.5] \times 10^{-8}$. This mode, together with Standard Model processes through a flavor-changing neutral-current (FCNC) interaction, are illustrated in Fig. 1.2. (Original plots and captions taken from [1])

1.2 The sgoldstino interpretation

Nearly a year later, D. S. Gorbunov and V. A. Rubakov [2] offered an interpretation where this intermediate state is a sgoldstino – one of the superpartners of goldstino, and one that can be light enough to be kinematically allowed in kaon decays.

This model where the light sgoldstino is a scalar particle predicts highly suppressed decays into muons [3], so it cannot explain the HyperCP result. Furthermore, in a model of a light pseudoscalar sgoldstino with *parity-violating* sgoldstino-quark couplings, a similar bound applies. On the other
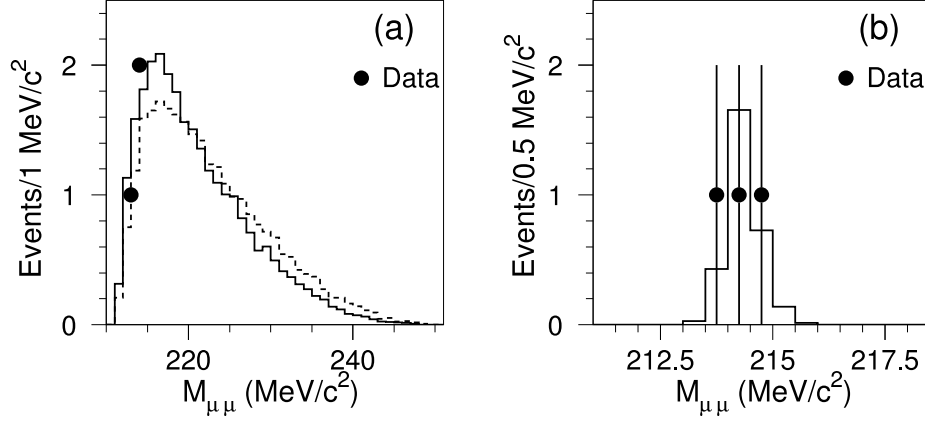
Figure 1.1: "Real (points) and MC (histogram) dimuon mass distributions for (a) $\Sigma^+_{p\mu\mu}$ MC events (arbitrary normalization) with a form-factor decay (solid histogram) and uniform phase-space decay (dashed histogram) model, and (b) $\Sigma^+_{pP\mu\mu}$ MC events normalized to match the data."
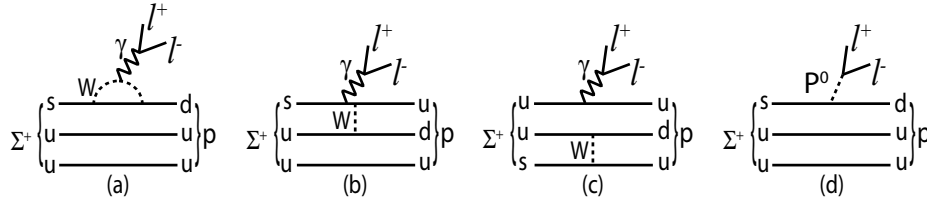
Figure 1.2: "Feynman diagrams for Σ^+_{pll} decays in the SM (a)–(c) and via new physics (d). The SM processes are referred to as FCNC (a) and internal conversion (b)–(c)"

.

1.2. THE SGOLDSTINO INTERPRETATION

hand, a pseudoscalar sgoldstino and models with parity conservation is the only remaining possibilty.

The corresponding Lagrangian for interactions between the pseudoscalar sgoldstino P and quarks is written [4]:

$$\mathcal{L}_{P,q} = -P \cdot (h_{ij}^{(D)} \cdot \bar{d}_i i\gamma^5 d_j + h_{ij}^{(U)} \cdot \bar{u}_i i\gamma^5 u_j) \tag{1.1}$$

or concerning flavour violating Pds couplings:

$$\mathcal{L}_{Pds} = -P \cdot (h_{12}^{(D)} \cdot \bar{d} i \gamma^5 s + h.c.) \tag{1.2}$$

where

$$h_{12}^{(D)} = \frac{1}{\sqrt{2}} \frac{\tilde{m}_{D,12}^{(LR)2}}{F} \tag{1.3}$$

relates to the energy scale of supersymmetry breaking, $\sqrt{F}$. Thus the constraints on sgoldstino couplings could translate into limits on $\sqrt{F}$.

The various branching ratios of kaons decaying into pions and P, now called X, are then estimated. Particularly, $\mathcal{B}(K_L^0 \to \pi^0\pi^0 X(X \to \mu^+\mu^-))$ is predicted to be 1.2×10^{-8} in the case $Re[h_{12}^{(D)}] \simeq |h_{12}^{(D)}|$. Furthermore, for $A_\mu \sim \alpha_2 M_{\gamma\gamma}$, $\mathcal{B}(K_L^0 \to \pi^0\pi^0 X(X \to \gamma\gamma))$ is expected to be 10^4 higher at 1.2×10^{-4}.

The upper bound to the lifetime of X is estimated using the vertex resolution and γ factors of the muons from the observed events in HyperCP. The lower bound is implied by:

$$\Gamma(P \to \gamma\gamma) = \frac{m_P^3 M_{\gamma\gamma}^2}{32\pi F^2} \tag{1.4}$$

in the unitarity limit when $M_{\gamma\gamma} \sim \sqrt{F}$. Overall the limits on the lifetime of X is:

$$1.7 \cdot 10^{-15}s \lesssim \tau_P \lesssim 2.5 \times 10^{-11}s \tag{1.5}$$

Because of the higher probability (taken to be unity) of decaying into photons, the X particle is best searched by its daughter photons. However the HyperCP experiment lacks photon detection ability, which gives us a chance to test out this theory. We therefore follow this interpretation in the analysis.

3

1.3 The Higgs boson interpretation

Another interpretation of the HyperCP result is provided by X. G. He, J. Tandean and G. Valencia [5]. In this theory, the next-to-minimal supersymmetric standard model (NMSSM) contains more than one Higgs particle. Among them, the lightest pseudoscalar A_1^0 can satisfy all existing constraints from kaon and B-meson decays, and may be identified with X.

The theory predicts the X decay is completely dominated by the muon-antimuon mode and assumes $\mathcal{B}(X \to \mu^+\mu^-) \sim 1$. Although we do not follow this interpretation, actually finding X in this analysis could mean that X is not a Higgs particle.

1.4 Hints at decay $K_L^0 \to \pi^0 X(X \to \gamma\gamma)$ - KTeV and NA48 experiments

The measurement of decay $K_L^0 \to \pi^0\gamma\gamma$ was reported by the KTeV collaboration in 1999 [6]. Upon closer inspection of the $m_{\gamma\gamma}$ plot, close to 200MeV there are 15 observed events compared to around 8 expected backgound events. This hints a possible decay $K_L^0 \to \pi^0 X(X \to \gamma\gamma)$, and when scaled to the $2\pi^0$ events ($\sim 4 \times 10^5$) in the same figure, corresponds to $\mathcal{B}(K_L^0 \to \pi^0 X) \sim 10^{-8}$.

On the other hand, the NA48 experiment published results of the same mode later in year 2002 [7]. From the $m_{\gamma\gamma}$ plot in this article (Fig. 1.4), there are no obvious excess events near 200 MeV.

However, neither experiment has published a re-analysis of the data specifically in the mass region of our hypothetical X particle. Thus, the subtle differences we note here give us a window of opportunity to search for the X particle.

1.5 K mesons

K mesons are bound states of a strange quark and either an up or a down quark. The "V events" were first observed by Rochester and Butler (1947) in a cloud chamber. In later researches, a mystery arose to what was known as the $\tau-\theta$ puzzle: The particle τ^+ decayed into $\pi^+ + \pi^+ + \pi^-$, while θ^+ decayed
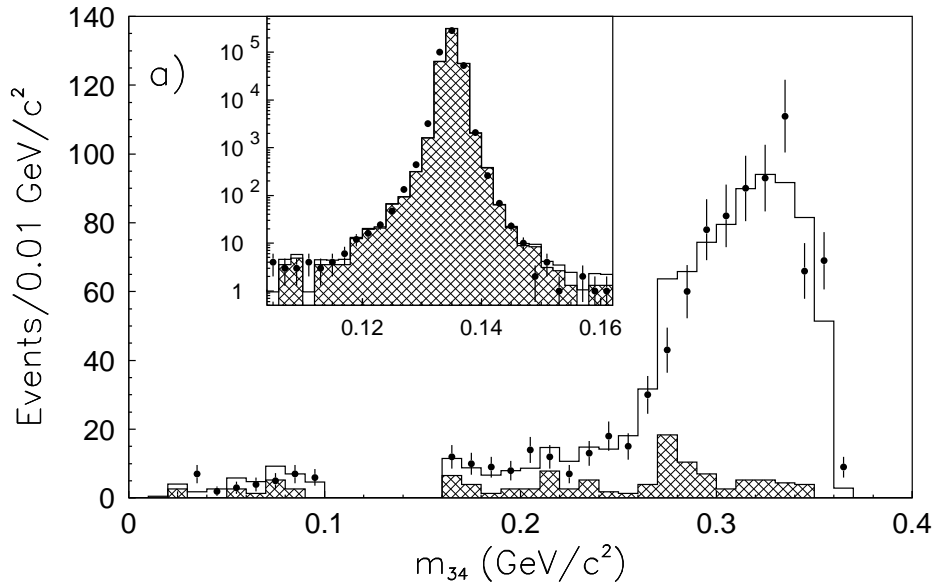
Figure 1.3: $m_{\gamma\gamma}$ plot, KTeV result in measuring $K_L^0 \to \pi^0\gamma\gamma$. Close to 200MeV there are $\sim$7 excess data events.

into $\pi^+ + \pi^0$, their final states having different parity. But with increasingly more precise measurements, τ and θ were found to have the same mass and lifetime, which meant they were the same particle. This puzzle was later solved by the discovery of parity violation in weak decays.

The K mesons consist of a strange quark and either an up quark or a down quark. The exact quark contents and other properties are listed in Table 1.1. (Data from Particle Data Group, PDG [8])

The neutral K mesons $K^0/\bar{K}^0$, are mutual anti-particles and are eigenstates of strangeness S and isospin I. However, they *always* decay to nonstrange particles, such as pions and leptons, via weak interactions that violate S but conserve CP (Charge conjugation · Parity transformation). Also, both K^0 and $\bar{K}^0$ can decay to 2π or 3π by weak interaction, so *mixing* can occur via virtual intermediate pion states, where a K^0 turns into a $\bar{K}^0$ and vice versa in a $\Delta S = 2$ transition.

This means, while in production we have definite states of either K^0 or $\bar{K}^0$, through propagation we'll always end up with their mixtures, which then decay weakly as CP eigenstates that we call K_{Long}^0 and K_{Short}^0. "Long" and "Short" here reflect the respectively longer and shorter lifetimes of the CP-
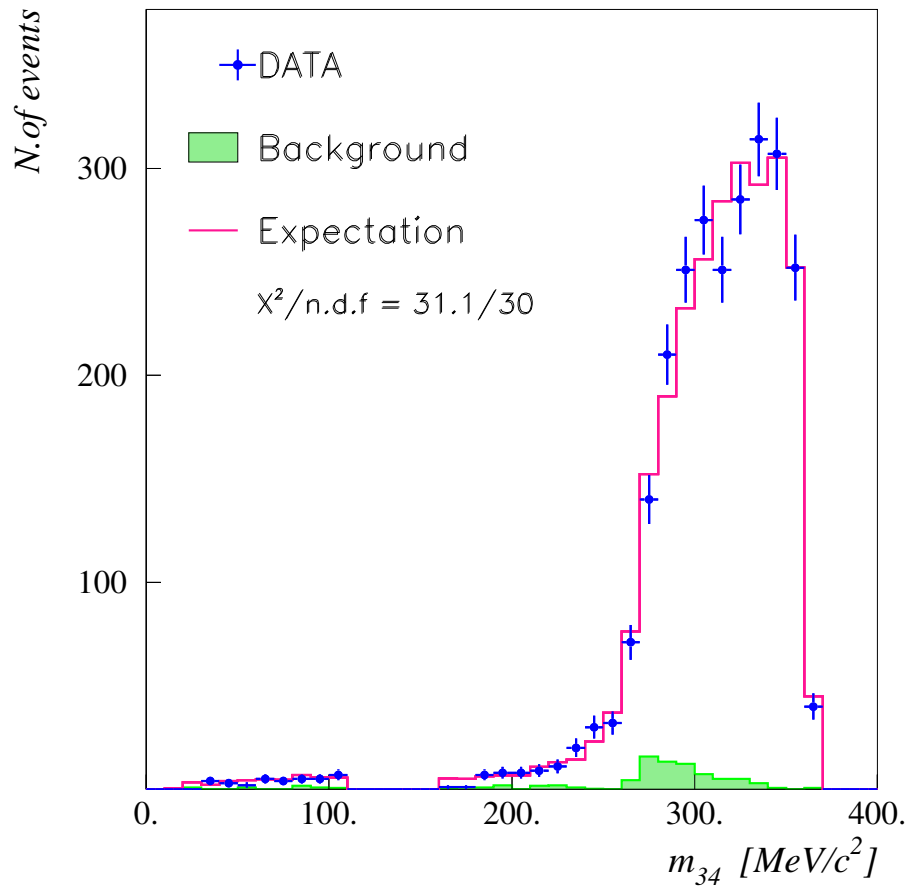
Figure 1.4: $m_{\gamma\gamma}$ plot, NA48 result in measuring $K_L^0 \to \pi^0\gamma\gamma$. No excess in signal

Table 1.1: The properties of K mesons

		Mass (MeV)	Lifetime (s)
K^+/K^-	$(u\bar{s}/\bar{u}s)$	493.677 ± 0.016	$(1.2385 \pm 0.0024) \times 10^{-8}$
$K^0/\bar{K}^0$	$(d\bar{s}/\bar{d}s)$	497.648 ± 0.022	
K_L^0(CP=-1)	$\frac{1}{\sqrt{2}}(K^0 - \bar{K}^0)$		$(5.114 \pm 0.021) \times 10^{-8}$
K_S^0(CP=1)	$\frac{1}{\sqrt{2}}(K^0 + \bar{K}^0)$		$(0.8953 \pm 0.0005) \times 10^{-10}$

Table 1.2: Relevent K_L^0 decay modes

	Modes	Fraction
Semileptonic	$\pi^{\pm}e^{\mp}\nu_e$	$(40.53 \pm 0.15)\%$
	$\pi^{\pm}\mu^{\mp}\nu_\mu$	$(27.02 \pm 0.07)\%$
Hadronic	$3\pi^0$	$(19.56 \pm 0.14)\%$
	$\pi^+\pi^-\pi^0$	$(12.56 \pm 0.05)\%$
	$\pi^+\pi^-$	$(1.976 \pm 0.008) \times 10^{-3}$
	$\pi^0\pi^0$	$(8.69 \pm 0.04) \times 10^{-4}$
Hadronic /w photon	$\pi^0 2\gamma$	$(1.49 \pm 0.08) \times 10^{-6}$

odd and CP-even states. The mixed states and their lifetimes are also listed in Table 1.1, while decay modes of our primary particle of interest, K_{Long}^0, is listed in Table 1.2 (PDG).

1.6 Thesis outline

In this thesis, the KEK-PS proton synchrotron and the E391a detector are presented in chapter 2. In chapter 3, I describe the Monte Carlo simulation. Chapter 4 details the analysis of $K_L \to \pi^0 X$, while chapter 5 deals with signal extraction techniques. I conclude in chapter 6 and give future prospects.

Chapter 2

KEK E391a

2.1 Introduction

The E391a experiment is the first dedicated search of the decay mode $K_L \rightarrow \pi^0 \nu \bar{\nu}$, proposed by T. Inagaki in 1996 [9]. It uses the KEK proton synchrotron to strike protons on a target. Having charged secondaries swept away by magnetic fields, K_L and other neutral particles are trimmed into a pencil beam by a set of precision collimators. The generated K_L particles in the neutral beam then decay in the vacuum decay region inside the detector, where the product photons are detected by an electromagnetic calorimeter. Photons that do not hit the calorimeter are caught by a hermetic veto system, which then allows us to reject the corresponding event. Likewise, decays with charged particles can be rejected with charged particle vetoes.

This design philosophy of hermetic vetoing combined with the ability to precisely detect photons makes E391a a good experiment for the search of the light sglodstino.

2.2 The Neutral Beam

2.2.1 Particle Generation

The KEK proton synchrotron accelerates protons to 12GeV in 2 seconds. These protons are then extracted into the East Counter Hall within 2 seconds. The bunch of extracted protons during this 4 second period is called a "spill".

The target is made of platinum, measuring 60 mm in length (or $0.68\lambda_I$) and 8 mm in diameter. It shares the same axis with the neutral beam, while
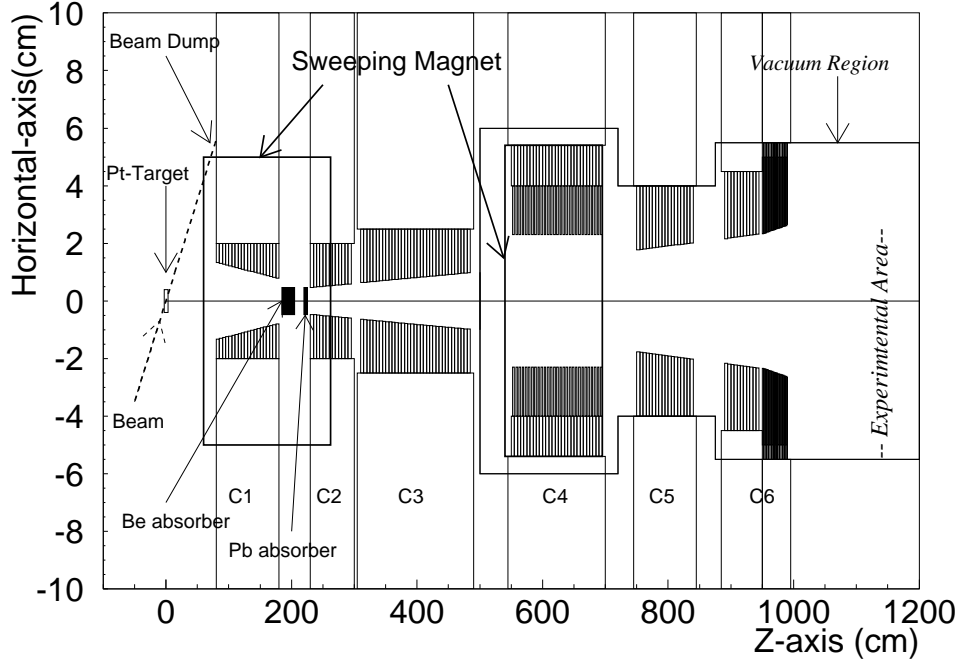
Figure 2.1: The beam line consists of 6 sets of collimators and a pair of sweeping magnets

the primary protons strike the target at 4 degrees horizontally off-axis of the intended neutral beam. This extraction angle helps improve number of K_L's versus neutrons. Non-interacting protons and high energy secondaries head straight into a 25 cm thick $(2.6\lambda_I, 71X_0)$ tungsten beam dump [10]. The ratio neutron/K_L is about 60 at this stage.

2.2.2   The Pencil Beam

A pencil beam means a narrow beam. With a narrower beam the event recon-struction can achieve a better transverse momentum resolution while assum-ing decay vertex on the beam line. The resolution for transverse momentum is important to the $K_L \rightarrow \pi^0 \nu\bar{\nu}$ mode as it relies on missing neutrinos (thus missing momentum) to discover signal. It is also a good criterion on event reconstruction quality for fully reconstructed modes (no missing particles), such as $K_L \rightarrow \pi^0 X$.

The narrow beam profile was achieved with 6 sets of collimators as shown

9
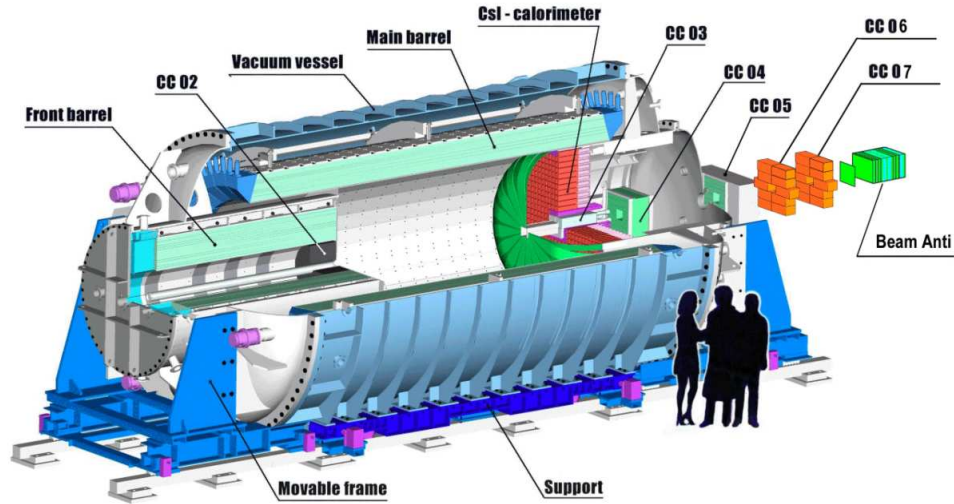
Figure 2.2: The E391a detector

in Fig. 2.1. The first 3 sets C1, C2 anf C3 define a half cone angle of 2mrad. C4 employs thin Gd_2O_3 sheets to reduce thermal neutrons, which are a source of accidental hits, by one order of magnitude [10]. C5 and C6 trim the beam halo to achieve $\sim 10^{-4}$ lower flux of halo neutrons and photons compared to the beam core [10]. Also shown in Fig. 2.1 are the Pb and Be absorbers, which reduce core γ's and neutrons respectively.

The beam enters the vacuum region at 11.8m downstream of the production target. This length helps reduce the number of punch-through muons and backgrounds from hyperon decays, such as $\Lambda \to n\pi^0$.

2.3   The E391a Detector

The detector is placed in the KEK East Counter Hall. Its measurements are shown in Fig. 2.3. The assembly is placed on a rolling rail track so the inside, which is completely covered except for beam entrance/exit, can be accessed by pulling the assembly apart. Concrete blocks are stacked around the detector to protect personnel from radiation. The control room and DAQ system are also inside East Counter Hall.

As shown in Fig. 2.2, the detector assembly is first recognized as a big cylindrical detector which is the Main Barrel photon veto, or MB. The MB
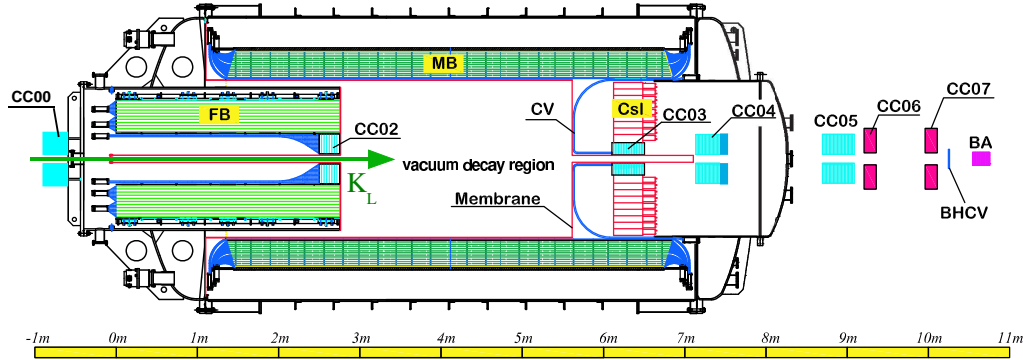
Figure 2.3: 2D view of the E391a detector

has another photon veto "plugged" into its front, which is called the Front Barrel (FB). It is then sealed at the rear with our primary detector, the CsI calorimeter. These 3 define a decay region inside. Collar Counters wrap around the beam both before and after the decay region, while Charged Vetoes cover the inside of the decay region to detect charged particles. The Back Anti at the extreme rear rounds out the system and serves as another photon veto.

2.3.1 Electromagnetic Calorimeter

<u>Overview</u>

In order to kinematically reconstruct decays, we use a grid of calorimeters to measure precisely the photons' energies and positions. The calorimeter as shown in Fig. 2.4 consists of a grid of pure CsI crystals arranged into a disk 1.9m in diameter, while leaving a 20cm × 20cm square hole in the center. Further inside is Collar Counter 3, or CC03, to be described later.

Two types of square-shaped CsI crystal are used. The majority are called "Normal CsI" and measure 7cm × 7cm × 30cm ($16X_0$). In order to fit a circular shape, some of these Normal CsI's are trimmed an angled surface (Fig. 2.5). These non-square crystals are called "Edge CsI" as they sit on the edges. The ones close to the center are narrower at 5cm × 5cm × 50cm ($27X_0$), which are borrowed from the KTeV experiment, hence called "KTeV CsI". There are 496 Normal, 56 Edge and 24 KTeV CsI's, or 576 crystals in total.

11
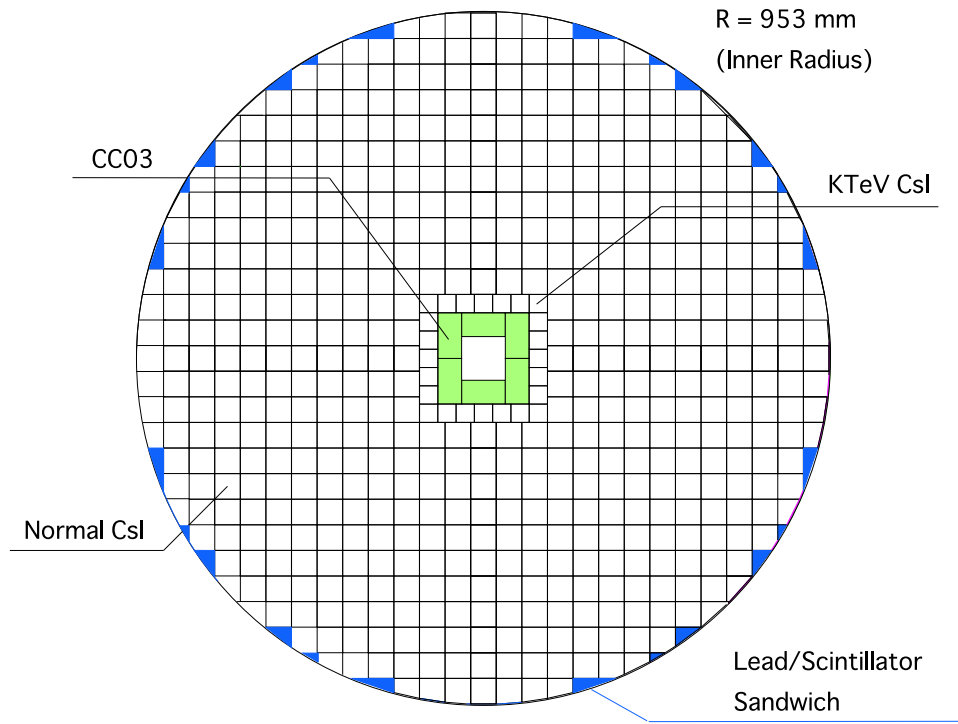
Figure 2.4: Overview of the Electromagnetic Calorimeter
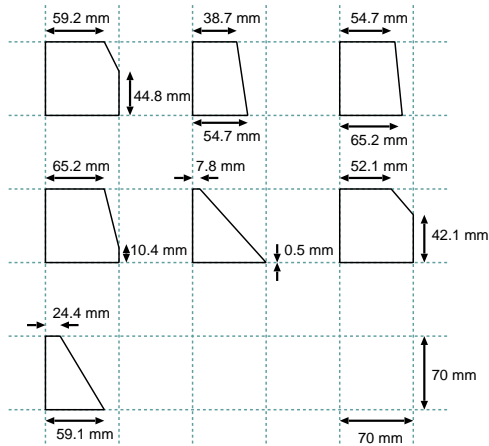
Figure 2.5: Edge CsI crystals in seven different shapes
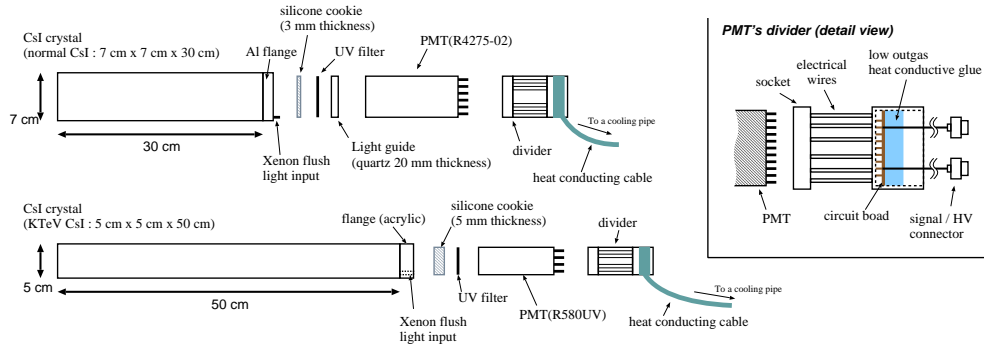
Figure 2.6: Schematic drawing of CsI modules and the PMT/divider config.

Implementation

The Normal CsI's are wrapped in 100 μm thick Teflon sheets, and further 20 μm Aluminized mylar. These wrappings optically isolate each crystal. Each Normal CsI is viewed by a PMT (2in Hamamatsu R4275-02) through a 5mm thick silicone cookie and a UV transmitting filter, which reduces the slow component of the scintillator light. One Normal CsI crystal has a yield of 15 photoelectrons per MeV energy deposit. In order to operate the PMT in vacuum, there had to be a large gap between the PMT and the divider. On the divider side, the current was reduced and heat conductive glue was applied to the circuit board. Heat was taken away by a cooling water pipe.

The Edge CsI's are similarly configured, although the 32 smaller crystals were viewed by $1\frac{1}{8}$in. Photonis XP 2978 PMT's instead.

The KTeV CsI's, which are smaller and situated at the inner edge, were wrapped with 13μm mylar. Each is viewed by a 1.5in. Hamamatsu R580-UV PMT and yield typically 20 photoelectrons per MeV of energy deposit.

Even with Edge CsI's there are gaps to be filled between crystals and the support structure. We use lead-scintillator sandwiches shaped in triangles of 3 different sizes as shown if Fig. 2.7. They have embedded WLS fibers to lead the signal to PMT's, where the other end is polished and aluminum coated. Typical light yield is 10-20 photoelectrons per MeV energy deposit. They are nicknamed SAND.

Energy calibration

The CsI's energy was calibrated by the following methods[11]:

•Electron beam incident on 5×5 stack of CsI.

13
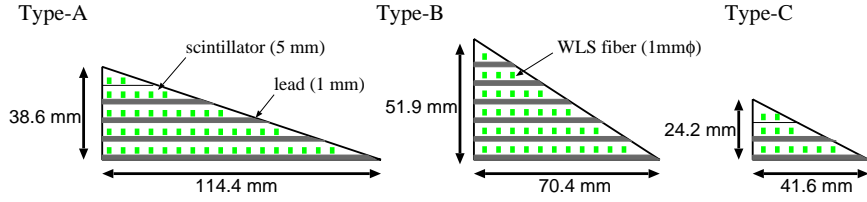
Figure 2.7: SAND detectors come in 3 different sizes to fill the gap.

•Cosmic muons with $5.63 MeV/cm$ energy deposits as MIP's.

•Punch-through muons from K_L beam with $170 MeV$ energy deposit.

•$m_{\gamma\gamma} = m_{\pi^0}$ from special π^0 run with aluminum generator, following (2.2).

•Constrained fit on $3\pi^0$ events, with 1 of 6 γ energies taken as unknown [12].

Resolution and efficiency

The energy resolution was measured using a positron beam incident on 25 Normal CsI crystals [13]. Fig. 2.8 shows this resolution in relation to incident energy. The result is:

$$\frac{\sigma_E}{E(GeV)} = \frac{1\%}{\sqrt{E(GeV)}} \oplus 1\% \tag{2.1}$$

The inefficiency due to photonuclear reactions was measured in an independent effort at KEK-Tanashi electron synchrotron [14]. This inefficiency was measured to be 10^{-4} at $E_\gamma = 100$MeV, and decreases to 2×10^{-7} at E_γ = 1GeV.

2.3.2   Charged Veto

Charged Veto (CV) refers to the umbrella shaped scintillator detector that spans in front of the CsI grid. As listed before, K_L decays predominantly into charged particles like $\pi^\pm e^\mp \nu_e$ or $\pi^\pm \mu^\mp \nu_\mu$. The CV is a powerful veto against these decays. The CV is grouped into the outer 32 panels of scintillator, and the inner 4 which are parallel to the beam (Fig. 2.9). Their downstream ends extend to outside of the decay region to be read by PMT's.
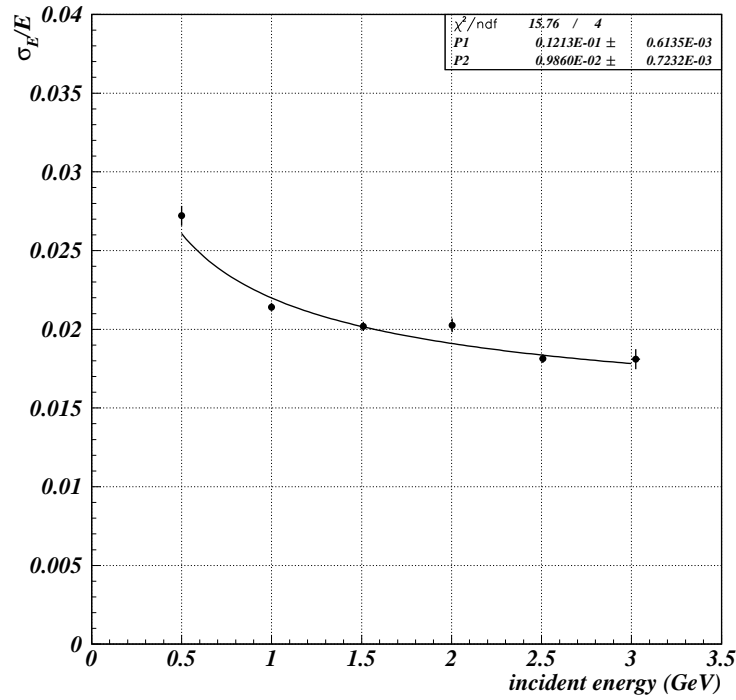
Figure 2.8: Energy resolution vs. incident energy as measured with a positron beam
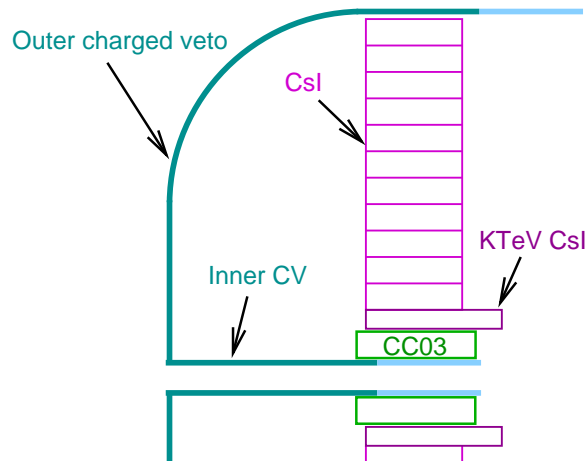
Figure 2.9: Outer and inner CV.
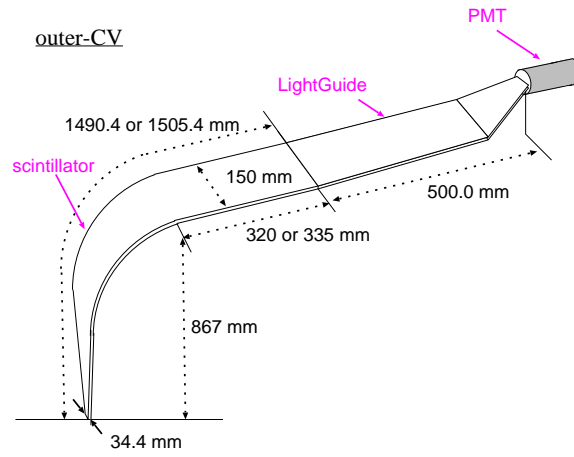
Figure 2.10: Detail of a single outer CV panel.
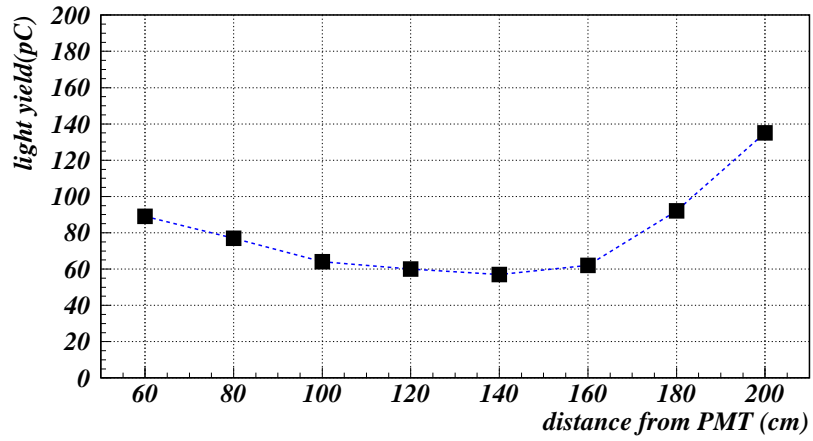
Figure 2.11: Outer CV light yield vs. distance from PMT.

16
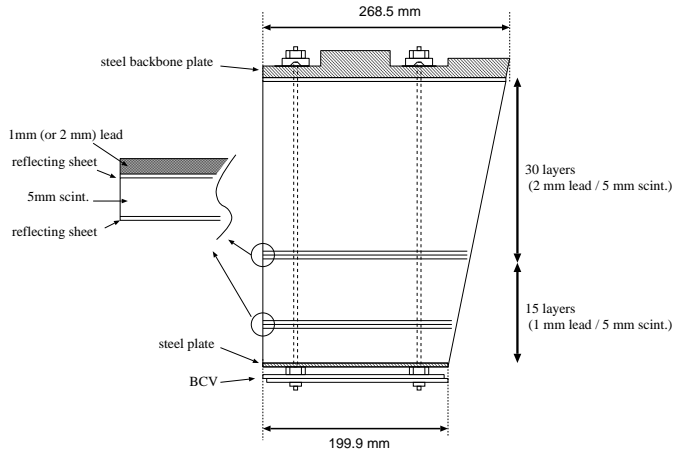
Figure 2.12: Schematics of an MB module. A module consists of 30 outer and 15 inner layers, while the innermost layer of scintillator is the Barrel Charged Veto (BCV).

2.3.3 Main Barrel

Main Barrel is a set of 32 modules shaped in skewed trapezoids and surrounding the decay region, which act as photon vetoes. Each module is divided into a 30-layer "outer" module and a 15-layer "inner" module (Fig. 2.12), and independently measured. Each layer consists of a lead-scintillator sandwich with a reflecting sheet at every interface, also shown in Fig. 2.12. The 15 inner layers have 1mm lead sheet each, while the outer 30 layers have 2mm lead sheets. MS resin was used for the scintillators instead of the usual polystyrene, due to the strength requirement of a long detector length.

The total thickness of one module is 317.9mm, or $13.5X_0$. The inefficiencies of this type of lead-scintillator sandwich are also measured at KEK-Tanashi electron synchrotron, and are found to be a factor of 2-3 higher than those of the CsI crystals [14].

Both inner and outer modules have scintillation light read at both upstream and downstream ends. Thus a module is viewed by four PMT's, which are of 2in types Hamamatsu R329-EGP. The PMT divider employs heat reducing techniques similar to those used on CsI crystals. The optical fiber readout scheme is shown as Fig. 2.14.

MB gain was monitored using a blue LED that flashed at 1.1Hz frequency. The gain shift was found less than 1% between on and off-beam periods. MB
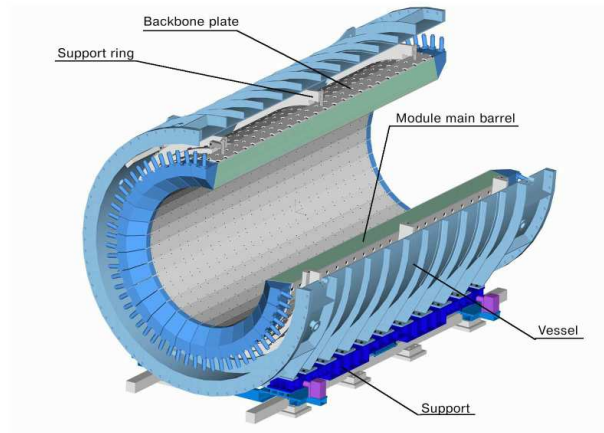
Figure 2.13: MB and BCV as installed on the supporting vacuum vessel.
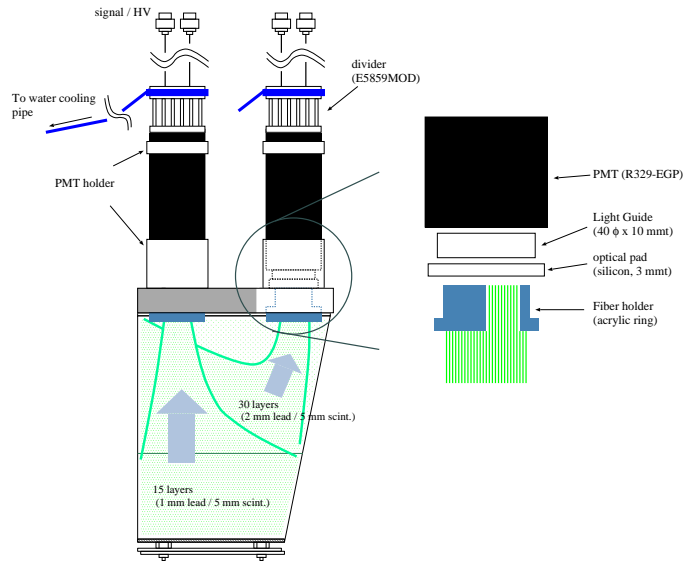
Figure 2.14: MB readout details (applied to both ends)
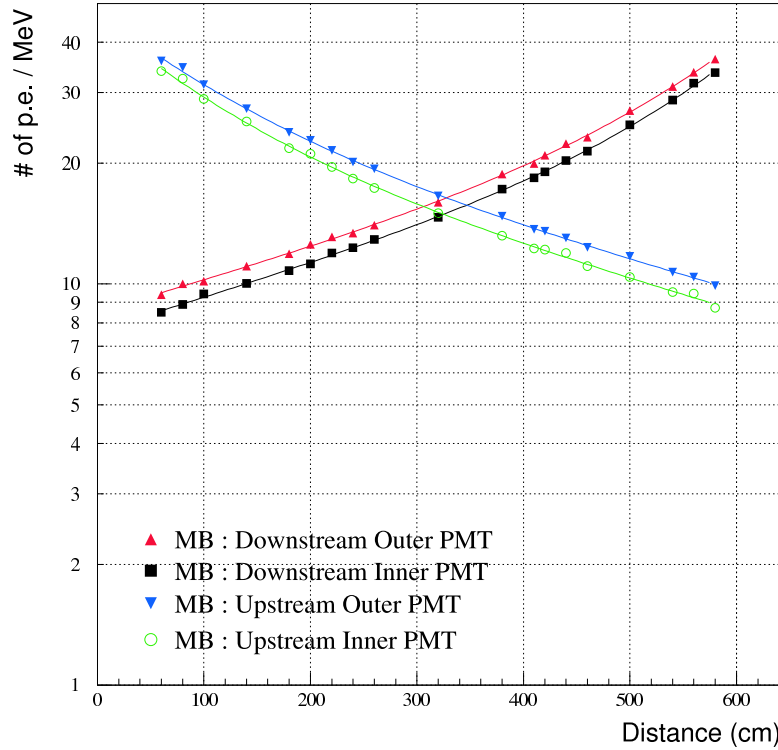
Figure 2.15: MB photoelectron yield vs. distance from PMT.

light yield was measured using cosmic muons, with $15/30 MeV/cm$ energy deposits for inner/outer modules [12]. The typical yield per MeV of energy deposit is 35 and 10 photoelectrons, for hits nearest and farthest to PMT respectively. See Fig.2.15. With this relation, the upstream and downstream readings of either inner or outer MB are combined to reclaim the true energy deposit at a later stage. The timing resolution is 0.6ns and 0.5ns for 15MeV (inner) and 30MeV (outer) respectively (Fig. 2.16)[15].

The Barrel Charged Vetoes (BCV, Fig. 2.12) are the plastic scintillator plates mounted on the inner surfaces of MB modules. They detect unwanted charged particles to provide for event vetoing. Each plate is wavelength shifting (WLS) optical fibers sandwiched between two 5mm scintillator plates, ending up 1cm in thickness (Fig. 2.17). They are also read from both up and downstream ends just like the MB.

19
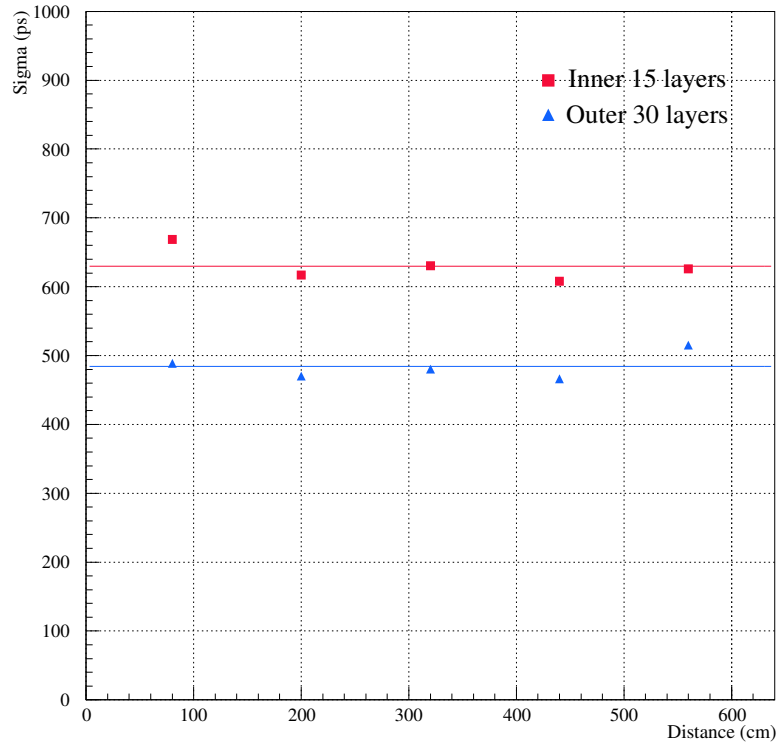
Figure 2.16: MB timing resolution (inner/outer) vs. distance from PMT
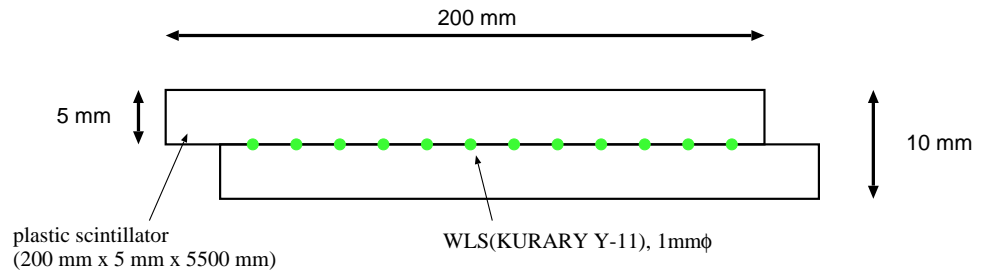
Figure 2.17: The BCV sandwich.

20
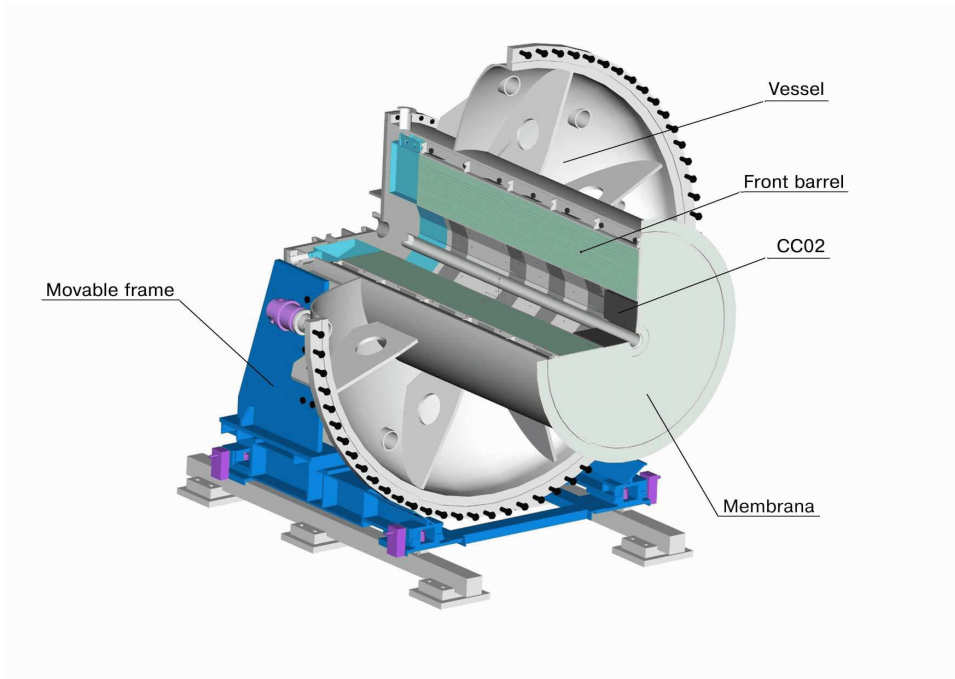
Figure 2.18: FB and the vacuum vessel/supporting structure.

2.3.4 Front Barrel

The Front Barrel (FB, Fig. 2.18) is similar to MB in construction and function, and surrounds the upstream part of the decay region. Its cylindrical shape has 1.45m outer and 0.62m inner diameter, while measuring 2.75m long. It consists of 32 separate modules read by PMT's at the upstream end. As shown in Fig. 2.19, each module has 59 pairs of 5mm scintillator plates and 1.5mm lead sheets divided into a 27-layer inner part and a 32-layer outer part, amounting to a total $17.2X_0$.

Cosmic ray muons are used to measure the performance of FB, both before and after installation. The light yield was found to be 20 and 10 photoelectrons, for hits at the nearest and farthest points to the PMT respectively.

National Taiwan University provided all the PMT's for MB and FB modules.
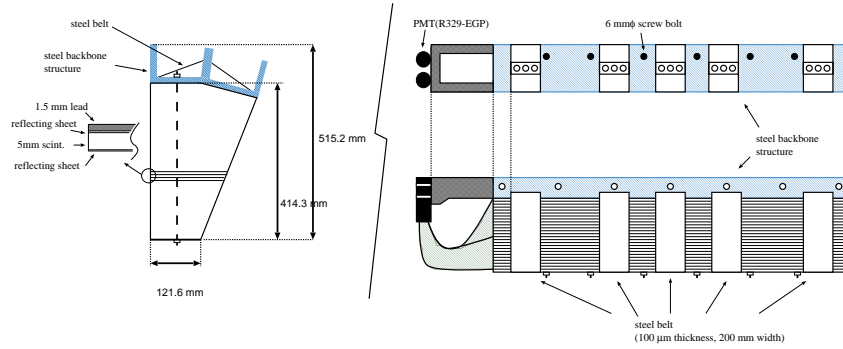
Figure 2.19: FB module, which consists of lead-scintilaltor sandwiches.

2.3.5   Collar Counters

Collar Counters detect photons that travel parallel to the beam. They closely surround the beam, hence the name. There were five collar counters: CC02∼06, but before E391a Run2 data taking, an extreme forward CC00 was installed. CC01 is absent due to historical reasons. The Collar Counters were calibrated by beam muons in special runs with the beam shutter closed. CC03, however, was calibrated similar to the CsI by cosmic muons.

CC00

CC00 is a new detector installed just before Run2 data taking. It is a tungsten alloy/scintillator sandwich located 85.5cm in front of the FB which consists of 10 layers of 2cm thick tungsten and 11 layers of 0.5cm thick scintillator, as shown in Fig. 2.20. This detector operates outside of the vacuum region. However, it has a central steel vacuum pipe with an inner diameter of 8cm.

CC02

CC02 is a ring of lead-scintillator sandwiches located inside FB, at the downstream edge. It consists of 8 modules, which are shaped to fit the FB on the outside and make an octagon on the inside, as shown in Fig. 2.21. Each module has 43 layers of 5mm scintillator and 1mm or 2mm lead sheet, for a total radiation length of $15.73X_0$. Light yield is 10 photoelectrons per MeV energy deposit.

CC03
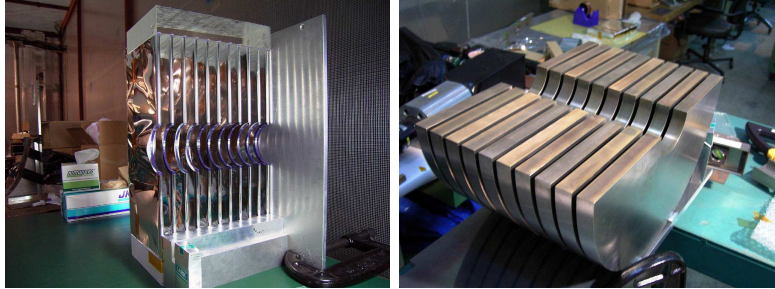
Figure 2.20: Half of CC00 (left: scintillator, right: tungsten)
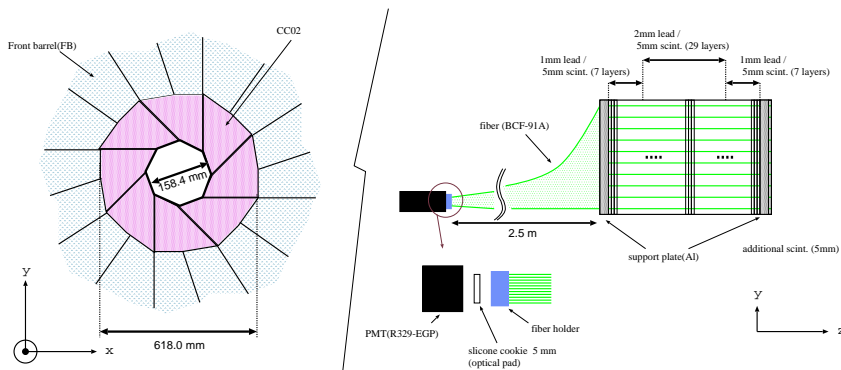
Figure 2.21: CC02 viewed from the downstream/ details and readout config.
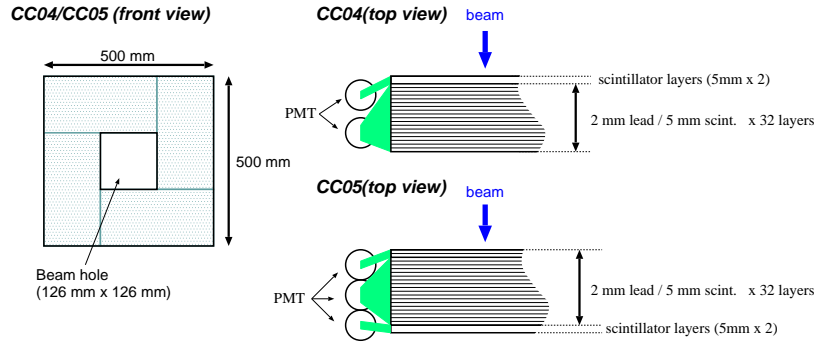
Figure 2.22: Front and top views of CC04/CC05.

CC03 as previously seen in Fig. 2.4 detects photons from high z decays, or decays near the CsI grid. To this end, these 1mm tungsten/ 3.4mm scintillator sandwich modules are oriented so the plates are parallel to the beam axis. They leave a 12cm × 12cm beam hole to the center.

CC04 & CC05

CC04 and CC05 are similar detectors downstream of the CsI grid, with schematics shown in Fig. 2.22. They both consist of 2mm lead/5mm scintillator layers, where CC04 has 2 5mm scintillators in the front with higher PMT gain, and CC05 has them in the back. Their total thicknesses amount to $11.4X_0$ each. Embedded WLS fibers allow direct PMT readouts.

CC06 & CC07

CC06 and CC07 are photon vetoes further downstream to CC05, and serve similar functions. CC06 and CC07 have identical structures as shown in Fig. 2.23. The lead glass that makes up the detectors has a composition of 55% PbO, 4% K_2O, 39% SiO_2 and 2% Na_2O, while the density is 4.08g/cm^3 and the refractive index is 1.7. This high refractive index allows electromagnetic showers to emit Cherenkov lights, which are then detected by PMT's attached with optical cement. Total radiation length is $6.3X_0$ for both.

2.3.6 Back Anti

Back Anti (BA) detects photons going through the beam hole of the CsI calorimeter. It sits at the end of the beamline and covers the beam core. This required a unique design because the BA would be subject to large
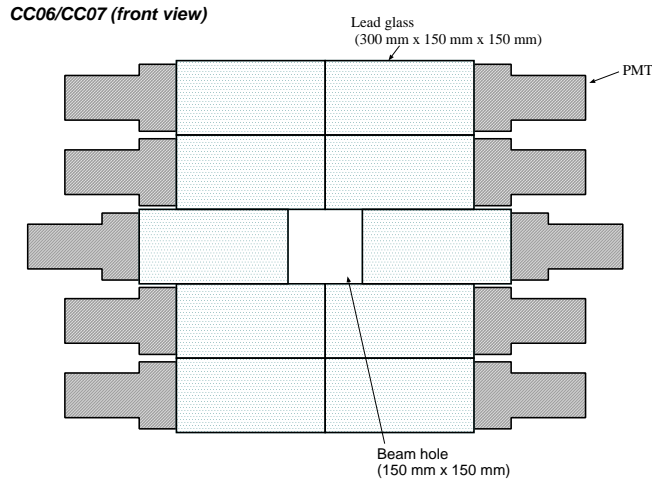
Figure 2.23: Both CC06 and CC07 consist of 10 lead glass crystals.

amounts of incident neutron, in addition to photons. This is accomplished by using both quartz crystals and scintillators, which give Cherenkov lights and scintillation lights respectively, constructed as shown in Fig. 2.24.

In operation, the secondary particles from neutron interactions are slower than the Cherenkov light threshold ($\beta=1/n$, where n=1.46 is the refractive index of the quartz crystals), so they do not give off Cherenkov light. But secondaries from both photons and neutrons deposit energy in the lead/scintillator sandwiches. By comparing signals from quartz and scintillators, we can discriminate between photons and neutrons. It has a total radiation length of $14X_0$.

2.3.7 Beam Hole Charged Veto

The Beam Hole Charged Veto rounds out the charged veto system. It also covers the beam core, and is composed of 4 partially overlapping plastic scintillator plates as shown in Fig. 2.25.

2.4 Vacuum System

Even after cleaning with collimators and absorbers, the neutral beam still contains considerable flux of neutrons. Should one of these neutrons collide with some air molecule, π^0's can be produced, which may in turn contribute

x

z

Beam

lead/scint. module
(6 lead sheets + 7 scint. sheets)

Quartz module
(7 quartz crystals)

30 mm

245 mm

35 mm

5 mm scint.   1mm lead

Beam

quartz crystal

Beam

WLS fiber

PMT

PMT
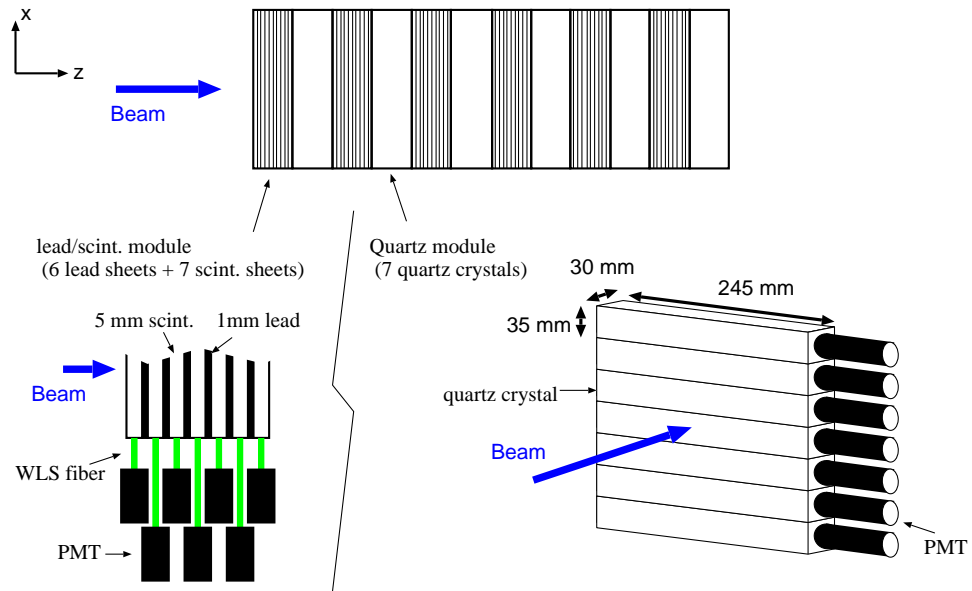
Figure 2.24: Upper: alternating layers of lead/scintillator and quartz. Lower: details of the two parts.

front view

Beam

Light guid

side view

PMT

Beam

50 mm

1 mm

200 mm
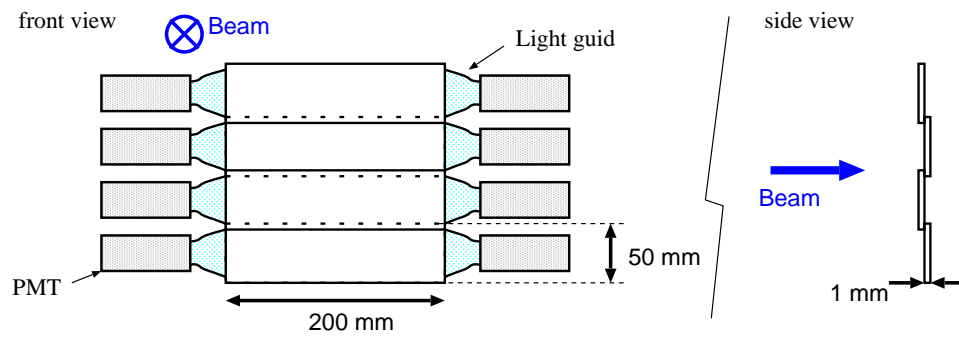
Figure 2.25: BHCV front view. / Side view showing the overlap.

26

Table 2.1: Specifications of vacuum regions

	Volume	Surface area	Operating pressure
Region-1	100 m^3	220 m^2	9×10^{-3}Pa
Region-2	10 m^3	40 m^2	1.7×10^{-5}Pa$\rightarrow 1.5 \times 10^{-5}$Pa

to the background for the mode $K_L \rightarrow \pi^0 \nu \bar{\nu}$, as it relies on a single recon-structed π^0 vertex to detect. To further suppress this effect, the decay region requires high vacuum of order 10^{-4}Pa [16]. Therefore, all detector compo-nents, except for CC00, CC05, CC06, CC07, BHCV and BA, operate in the vacuum.

2.4.1 Overview

However, the large out-gassing from the detector components interferes with the vacuum requirement. The problem is avoided by dividing the vacuum into two regions: one with the desired high vacuum of $< 10^{-4}$Pa (Region-2), and the other lower vacuum region (Region-1) of 0.01Pa which contains the detector components. This division is done with a 190μm ($4 \times 10^{-4} X_0$) thick "membrane". This membrane consists of ordered layers of polyethylene, aluminized EVAL, nylon and again polyethylene. Supported by aluminum tubes, it wraps the inner surface of the decay region. The vacuum system is shown in Fig. 2.26.

2.4.2 PMT operation in vacuum

By operating PMT's in vacuum, they cannot be cooled by convection and have to be water-cooled. In order to do so, copper pipes are are installed to the back of the CsI crystals, which have light yield sensitive to temperature, and 10°C cold water is run through the pipes as coolant. The PMT's dividers have heat conducting copper cables connected to the cooling pipes. During Run2 data taking, the CsI temperature remained close to 22°C. Water cooling was also used for FB, MB and BCV.
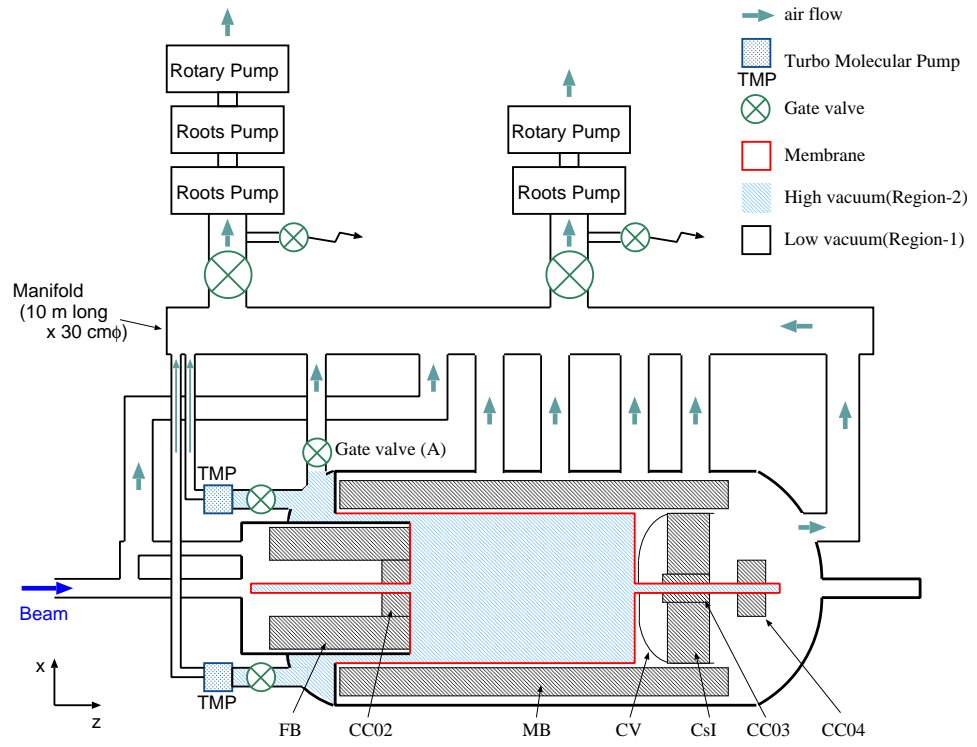
Figure 2.26: Schematics for the vacuum system, where Region-1 is in low vacuum and Region-2 is in high vacuum.

2.5 Triggering

2.5.1 AmpDiscri module

Triggering requires fast on-line cluster selection and veto logic. Also the timing information needs to be determined quickly. This is aided by the AmpDiscri module, or AD module, as shown in the upper left of Fig. 2.31.

The AD module takes 16 analog inputs corresponding to 16 channels of PMT voltages. Its output is threefold: a) pass-through of the original 16 channels un-modified, to be recorded as final energy readings later, b) two 8-channel analog sums, c) 16 timing informations of all channels according to a low threshold.

2.5.2 Physics trigger

To trigger the recording of a physics event, the Hardware Cluster Counter was used. As shown in Fig. 2.27, the CsI crystals were divided into 72 regions, each consisting of 8 adjacent crystals combined into 1 analog sum by the AD module as quick hardware clustering. The number of regions whose analog sum exceeds 30mV (approx. 60MeV energy deposit) are noted as N_{HC}. $N_{HC} \geq 2$ is required for a physics event to avoid taking beam associated events with $N_{HC} = 1$ (Fig. 2.28).

Other requirements are the "on-line vetoes", which are certain thresholds for allowed energy deposits (analog sums of 8-channel groups or total analog sums) in veto detectors. The requirements are listed in Table 2.2. Worthy of special notice is the very tight threshold for CV, which corresponds to 1MeV. This threshold is chosen to be below energy deposited by a minimum ionizing particle, so that the charged decay events are rejected. This on-line veto threshold on 8-channel sums cannot be precisely translated to final single channel readings.

Physics trigger rate

The typical physics trigger rate in Run2 data taking is about 400~500 per spill.

However, in Run1 data taking, the physics trigger rate was as high as 1000 per spill. This was due to the part of vacuum membrane, that covered the CV region, drooping down into the beam as shown in Fig. 2.29. The
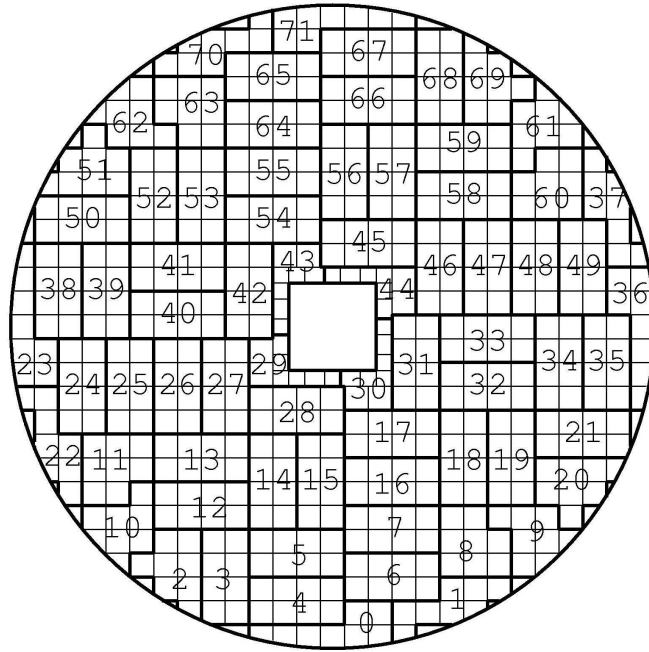
Figure 2.27: Groupings of 8 crystals into 72 regions for the Hardware Cluster Counter.
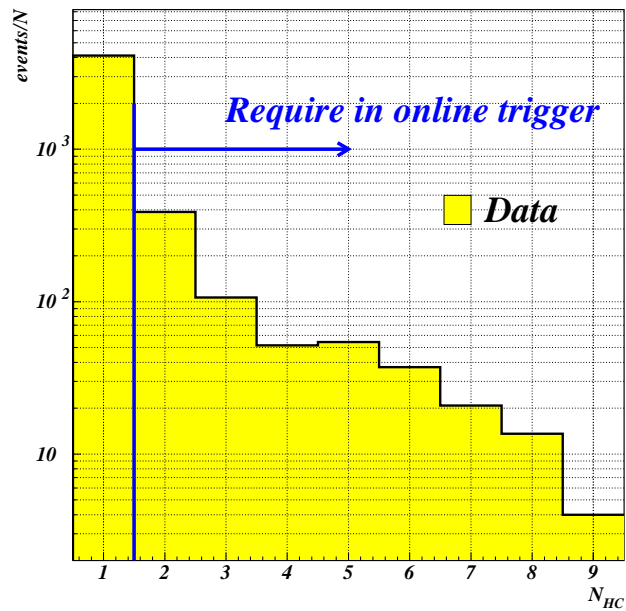
Figure 2.28: The large amounts of $N_{HC} = 1$ events were discarded.
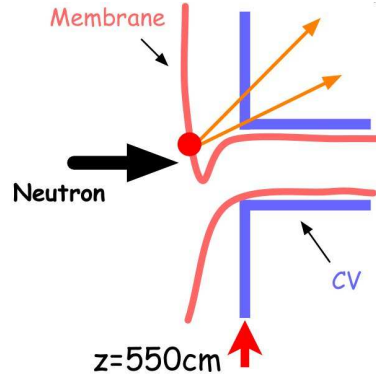
Figure 2.29: Neutrons striking the membrane, creating π^0 and fake events

Table 2.2: Detector thresholds for online vetoing.

Detector	Threshold (mV)	Equivalent MeV
CC03	-29	
MB	-31.2	30~40
ICV	-28.9	~1
OCV	-25.7	~1
CC02	-48.6	
CC04	-57.1	
CC05	-34.3	
FB	-100	

membrane was hit by neutrons, which then produced π^0's according to:

$$n + A \rightarrow \pi^0 + A' \tag{2.2}$$

π^0's then decayed into 2 photons caught by the CsI. This satisfied the condition for the physics trigger of 2 hardware clusters, and caused very high physics trigger rates and background to the $K_L \rightarrow \pi^0 \nu \bar{\nu}$ search, which relied on events with $N_{CLS} = 2$. It is fixed before Run2 data taking, as is evident from the lower trigger rate.
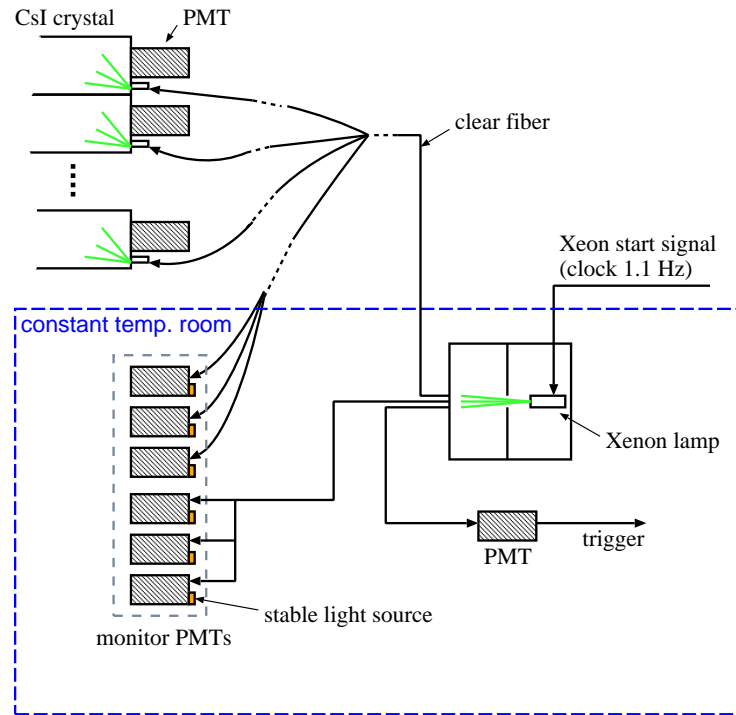
Figure 2.30: Calibrating CsI gain using the xenon lamp system.

2.5.3   Other triggers

Calibration trigger

For monitoring the CsI gain, a xenon trigger is used in conjunction with a xenon lamp flashing at 1.1Hz. 1.1Hz was chosen so as not to synchronize to the 2sec spill. Fig. 2.30 shows the gain monitoring setup. To monitor the MB gain, an LED trigger is used instead with LED's flashing at 1.1Hz. Cosmic trigger and muon trigger catch muons passing through vertically and horizontally respectively, to calibrate detector systems.

Minimum bias trigger

The performance of the physics trigger is checked by a set of triggers under relaxed conditions. One is requiring $N_{HC} \geq 1$ and the other requiring $N_{HC} \geq 2$, both without any on-line vetoing.

Accidental trigger

The many secondary particles entering the detector cause frequent background interactions, accidentally triggering detectors. These interactions

cannot be economically simulated using a Monte Carlo (MC) method. Instead, these accidental "hits" are separately recorded following an accidental trigger. Since accidental activity depends on beam intensity, this involves a detector located next to the production target and catches secondary particle emissions to identify a coming spill. The accidental hits in all detectors are recorded to paint a layer of background in the later analysis.

However, the accidental trigger, by operating independently of the physics trigger, cannot record accidental events exactly on-time with the physics event. Instead, the accidental trigger fires most often when proton intensity peaks, but physics decays can happen before or after the peak as well. Therefore, Monte Carlo decays usually end up being overlaid with accidental events taken at proton intensity peaks. This poses a bias in MC modelling of accidental detector energies.

2.5.4 Data Acquisition

The E391a DAQ system [17] consists of 2 Fastbus-VME systems and 1 TKO-VME system, which are then connected to a PC event builder via the GbE network. Also connected on the GbE network are online monitors, environment monitors and HV control. The event data is first buffered in the event builder PC, then transferred, after each run, to the KEK High Performance Storage System (HPSS). Typical filesize per day is 90GB.

In detail (Fig. 2.31), the 2 Fastbus-VME systems process ADC for all channels and multihit-TDC fo BA and BHCV, which takes a total processing time of 600μs per event including a conversion time of 256μs for ADC. The TKO-VME system, on the other hand, deals with all singlehit-TDC. The conversion time is 100μs, while the total processing time is 500μs. An 8-bit event ID was given to each of ADC, multihit-TDC and singlehit-TDC to ensure they process to the same event.

2.6 Data Sample

There are a total of three data taking Runs. Run1 data was taken from February to June 2004, has the highest statistics of all three Runs but was plagued by the drooping membrane problem mentioned earlier. Run2 data
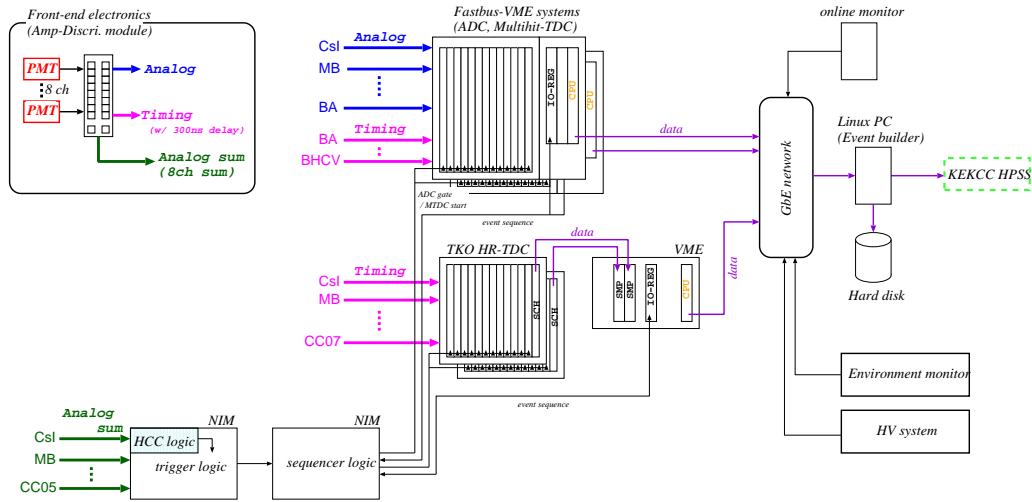
Figure 2.31: Schematics for the E391a DAQ system.

taking lasted from February to March 2005 for a total duration of two months. Run3 data was taken from October to December 2005. A new type of Back Anti (BA) was installed before Run3.

We use all available Run2 physics data in this analysis, which amounts to 417 "runs", where each "run" takes data for a period of about 2000 spills, and is manually started/ended.

2.6.1   Data taking shifts

I was fortunate enough to participate in Run3 data taking during the winter, 2005. One day of data taking was broken into three shifts of 8 hours' length each. During each shift, both the DAQ system and detector status were monitored in a control room just outside the detector's anti-radiation concrete blocks. The DAQ was started/ended manually in the control room while the beam operated continuously. After each run of about 2000 spills, a run summary was logged containing beam intensity, detector status, vacuum levels, targets used and temperature readings. Any problems encountered during the run was also written in the log book.

The most frequently occuring issue was a high voltage (HV) trip of one of the CsI PMT's. Once tripped, the HV had to be turned off and back on, the run had to be stopped and a new run would start. The beam itself went down a few times, but the beam operators could always bring it back on line

quickly. There was also an earthquake that caused the beam intensity to be unstable for a while.

Chapter 3

Monte Carlo Simulation

To study the efficiencies of the signal, normalization mode and backgrounds, a Monte Carlo (MC) simulation is used. The Geant3 package forms the backbone of our MC simulation, including both particle decays and detector interactions [18].

The product of the MC simulation has both timing information and energy deposits converted to the same format as real data. This allows us to treat MC and data using exactly the same selection criteria.

3.1 Particle generation

In order to save processing time, the parent K_L particles are generated at the exit of collimator 6, the last collimator, instead of the target. The K_L has its initial radial position and momentum vector generated according to their respective distributions, which are obtained from an independent "beamline simulation".

The final momentum distributions, however, are further fine tuned to match the real data once data samples became available, using the very clean and well-reconstructed $3\pi^0$ mode [19]. The tuning is an iterative process of repeated comparing reconstructed MC and data, then modifying generating distribution functions. The MC tuning results are shown in Fig. 3.1.

Figure 3.1: MC tuning result, $K_L \to 3\pi^0$ mode (dot with error bar: data, histogram: $3\pi^0$ MC)

3.2 K_L propagation and decay

The generated K_L has the decay point determined by its momentum p_{K_L}, proper time τ and the Lorentz factor. More precisely, the decay distance z from the target is distributed as:

$$f(z) \propto exp(-\frac{z}{\Delta z}) \tag{3.1}$$

where

$$\Delta z = c\tau\beta\gamma = c\tau \times \frac{p_{K_L}}{m_{K_L}} \tag{3.2}$$

Once the K_L propagates to the decay point it vanishes, and the secondary particles are generated in the K_L rest frame, according to Geant3 internal modes or through user defined modes. The secondary particles then decay to tertiary particles in their respective rest frames after similar propagation. The tertiary particles are Lorentz boosted to the K_L rest frame, and then further boosted back to LAB frame.

3.3 Decay modes and statistics

Although Geant3 supports mixed-mode generation according to correct branching ratios, in practice different modes were generated separately with 100% branching ratios. This separated MC generation allows important modes to receive accordingly higher statistics.

37

The decay modes considered in this analysis are listed below:

$\underline{K_L \to 2\pi^0 \text{(Normalization/Background)}}$

This mode is included in Geant3.

$\underline{K_L \to 3\pi^0 \text{(Background)}}$

This mode is included in Geant3.

$\underline{K_L \to \pi^0 \gamma\gamma \text{(Background)}}$

This mode was not included in Geant3. I had to manually put the generator in the simulation. This mode is special in that the di-γ invariant mass follows a specific distribution according to the Chiral Perturbation Theory [20]. Details are provided in Appendix A.

$\underline{K_L \to \pi^0 X \text{(Signal)}}$

This mode was not included in Geant3. I put generators for each of the four hypothetical target m_X's (discussed in Chapter 4) in the simulation. In this mode, the K_L is asked to decay into a π^0 with $m_{\pi^0} = 134.9766$ MeV and an X with fixed mass $m_X = 181.7, 198.0, 214.3, 230.6$ (MeV), where both the pion and the X particle decay immediately into two photons each. Since we have no width information for particle X, this fixed m_X decay allows us to probe mass resolution instead.

3.3.1 Statistics

The overall generated MC statistics, as well as comparison to Run2 data set, is listed in Table 3.1. The $K_L \to 3\pi^0$ mode suffuers from too low statistics compared to data. However, the sample already took three months to generate, which means it could take a year to generate the amount equal to data. It is difficult to overcome this limitation without more computing power.

3.4 Energy deposit

Geant3 allows particle interactions with all detector materials to generate showers. Secondary particles are traced until a low energy limit is reached. The limit is 0.05MeV for electrons, positrons and photons; 0.1MeV for hadrons and muons. The total energy in the sensitive parts of detector components are summed into the final energy.

Table 3.1: MC statistics

Mode	# of K_L's at C6	% of Run2 data set
$K_L \to 2\pi^0$	2×10^9	10 times
$K_L \to 3\pi^0$	1×10^{10}	25%
$K_L \to \pi^0\gamma\gamma$	7.5×10^7	240 times
$K_L \to \pi^0 X(\text{each})$	7.5×10^7	N/A

However, because the Main Barrel (MB) is very long and the Charged Veto (CV) is shaped differently, their "energies" are treated somewhat differently to reflect internal light propagation/attenuation:

MB

Due to the length of the MB, there's an observed exponential attenuation of scintillation light as it propagates along the length of the MB. Also, the propagation time for light to travel to upstream and downstream PMT's needs to be simulated.

The attenuated energy reaching the PMT, for a hit at a distance l away, is modelled by:

$$E = E_0(a_1 e^{-\frac{l}{\lambda_1}} + a_2 e^{-\frac{l}{\lambda_2}}) \tag{3.3}$$

where the attenuation lengths are measured with cosmic muons (as shown in Fig. 2.15): $\lambda_1 = (6.08 \pm 0.56)m$ (long term) and $\lambda_2 = (1.13 \pm 0.15)m$ (short term), while $a_1/a_2 = 1.11 \pm 0.02$ [15]. The total scale, however, is fixed by defining the energy deposit of a minimum ionizing particle, which strikes the MB's midpoint, to be 15 MeV and 30 MeV as read by the PMT for Inner and Outer modules respectively.

The light propagation time is modelled using a propagation speed of $(17.7 \pm 0.1)cm/nsec$, obtained from cosmic muon measurements [15].

CV

As shown in Fig. 2.11, the CV's wedged shape creates a perculiar dependence of photoelectron yield on hit position. This dependence is used in MC generation.

3.5 Accidental activity

Accidental activities, as mentioned in section 2.5.3, can both affect event efficiency and cause fake clusters. Accidentals arise due to various interactions with detector materials from secondary particles in the beam, along with our desired kaons. These activities are too numerous to simulate effectively, so we use an accidental overlay method, with accidental activities recorded during data taking.

The accidental trigger fires according to beam intensity, and accidental events are recorded separately from K_L decays. These events are directly overlaid on top of the "pure" MC samples, in effect adding noises to all detector channels. Energy for a particular channel is the sum of pure and accidental energies, while timing is decided by the earlier time between them.

3.6 Combination of modes

Because the MC for different modes are not generated in proportion to their respective branching ratios, they require certain weighting factors before combining. The combined background MC is in the form:

$$MC^{total} = \sum_{mode} MC^{mode} \times A^{mode} \tag{3.4}$$

where

$$
\begin{aligned}
A^{2\pi^0} &= \mathcal{B}(K_L \to 2\pi^0)/N_{generated}^{2\pi^0} \\
&= (4.345 \pm 0.020) \times 10^{-13} \\
A^{3\pi^0} &= \mathcal{B}(K_L \to 3\pi^0)/N_{generated}^{3\pi^0} \\
&= (1.956 \pm 0.014) \times 10^{-11} \\
A^{\pi^0\gamma\gamma} &= \mathcal{B}(K_L \to \pi^0\gamma\gamma)/N_{generated}^{\pi^0\gamma\gamma} \\
&= (1.99 \pm 0.11) \times 10^{-14}
\end{aligned}
$$

calculated with branching ratios taken from PDG values, and $N_{generated}^{mode}$ from Table 3.1.

However, we use the mode $K_L \to 2\pi^0$ as normalization so it is convenient to scale all modes to it, and re-writing (3.4) as:

$$MC^{total}_{normalized} = MC^{2\pi^0} + \frac{A^{3\pi^0}}{A^{2\pi^0}} \times MC^{3\pi^0} + \frac{A^{\pi^0\gamma\gamma}}{A^{2\pi^0}} \times MC^{\pi^0\gamma\gamma} \tag{3.5}$$

Chapter 4

Analysis Method

4.1   Introduction

The search for $K_L \to \pi^0 X$ is performed over a range of four hypothetical m_X: 181.7MeV, 198.0MeV, 214.3MeV and 230.6MeV. These equally spaced mass values span the mass spectrum higher than π^0 mass peak and lower than the kinematical bound. They also serve as mutual verification for possible systematic errors. These target "particles" and their respective analyses will be referred to as $X_{181.7}$, $X_{198.0}$, $X_{214.3}$ and $X_{230.6}$.

To this end, event selection was separately optimized for each hypothetical target signal. Four independent analyses were performed on the same data and MC sample, only with different generated mass for the signal MC. We extract the signal (N_{sig}^{obs}) from each set of analysis.

The branching ratio would then be calculated by:

$$\mathcal{B}(K_L \to \pi^0 X) = N_{sig}^{obs} \times \frac{1}{N_{decay} \times A_{sig}} \tag{4.1}$$

where $\frac{1}{N_{decay} \times A_{sig}}$ is the Single Event Sensitivity, or S.E.S. In practice, however, the *ratio* of $\mathcal{B}(K_L \to \pi^0 X)$ to $\mathcal{B}(K_L \to 2\pi^0)$ is measured as:

$$\frac{\mathcal{B}(K_L \to \pi^0 X)}{\mathcal{B}(K_L \to 2\pi^0)} = \frac{N_{sig}^{obs}/A_{sig}}{N_{2\pi^0}^{obs}/A_{2\pi^0}} \tag{4.2}$$

This permits simultaneously measuring $K_L \to 2\pi^0$ and $K_L \to \pi^0 X$ on an almost equal footing. Then, the Particle Data Group (PDG) value for $\mathcal{B}(K_L \to 2\pi^0)$ is substituted in to extract our desired $\mathcal{B}(K_L \to \pi^0 X)$.

4.2 Event Reconstruction

In an E391a analysis, events are first sorted by the number of clusters, or N_{CLS}, formed on the CsI grid by EM showering. Due to strong on-line vetoing on the Charged Vetoes, only decay modes with all product particles neutral can be considered. The event is then kinematically reconstructed by first assuming K_L decay vertex on the beam axis, thanks to a pencil beam line. This is followed by assuming known kaon and/or pion mass to determine the decay z, which then allows full reconstruction of kinematic variables. Event selection relies heavily on kinematic variable cuts, in addition to veto and clustering information.

4.2.1 Clustering routine

The data comes in the form of energy readings of individual crystals. In order to find the energies and positions of the incident photons, they must be grouped into clusters. Ideally a cluster should represent the electromagnetic shower from a single photon.

We define crystals with energy above 5MeV as "cluster seeds". We begin by finding the neighboring crystals to the seed of the highest energy. The cluster forms by including subsequent neighbors with energy deposits until no other such neighbor exists. Then the remaining "cluster seed" with the highest energy is used to grow into another cluster. This process repeats until all seeds are exhausted, either grown into their own clusters or taken into clusters formed by seeds of higher energy.

Then, in order to reject non-isolated clusters, all clusters are required to have a single local maximum in energy. A maximum is a crystal with higher energy than all its neighbors sharing a side. A non-isolated cluster having more than one maximum may be formed by mutiple photons, and events containing such clusters are discarded. This rejection was found, with a MC study, to cause 15% and 8% acceptance losses to $K_L \rightarrow 3\pi^0$ and $K_L \rightarrow 2\pi^0$ decays repsectively, due to the possibility of a single photon creating mutiple maxima.

The incident position is found as the center of energy (COE):

$$x_{COE} = (\sum_i x_i E_i)/E_{cluster} \tag{4.3}$$

KTeV crystals

CC03

35x35 cm²

R = 80 cm
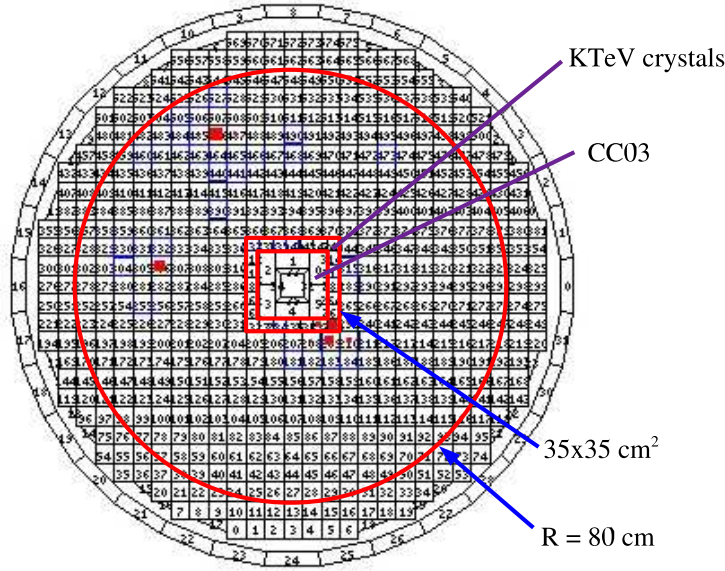
Figure 4.1: "Sqaure-Holed Coin" selection for cluster positions

which is to be corrected later to account for position shifting in angled inci-
dents.

The decay $K_L \to \pi^0 X$ has a final state of 4 photons, which should gen-
erate 4 clusters if all 4 strike the CsI, as mentioned in Chapter 2. Only
$N_{CLS} = 4$ events are considered.

To avoid taking clusters with lateral shower leakage out of CsI crystals,
all clusters must lie inside a circle with $R = 80cm$ and outside the central
square formed by the "KTeV" crystals at $35 \times 35cm^2$. This "Square-Holed
Coin" selection is shown in Fig. 4.1.

4.2.2 Kinematic reconstruction

The process of full kinematic reconstruction is shown as the flow chart Fig.
4.2, and is described in detail as follows.

<u>Photon pairing</u>

Because both π^0 and X decay to a pair of photons, the four resultant
photons can have six different "pairing" configurations, as shown in Fig. 4.3,
where only one "pairing" corresponds to the true decay relationship. All six
pairings are separately reconstructed in the following procedures.
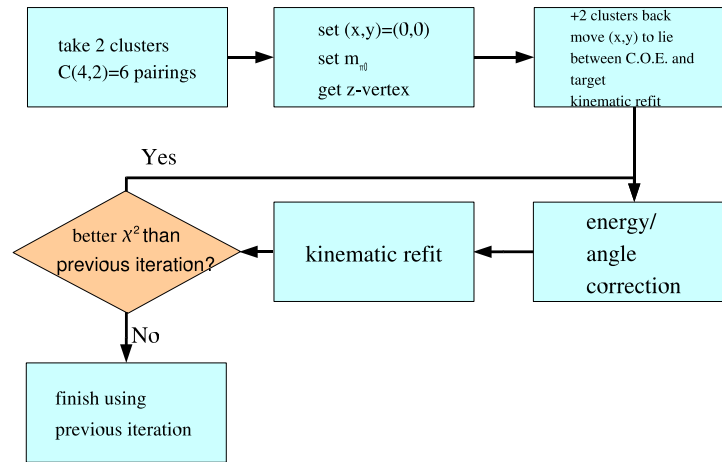
Figure 4.2: Flow chart for kinematic reconstruction
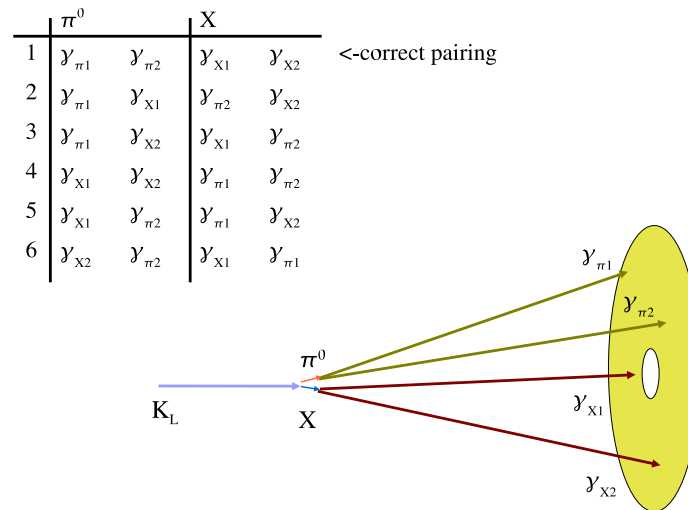
Figure 4.3: γ pairing
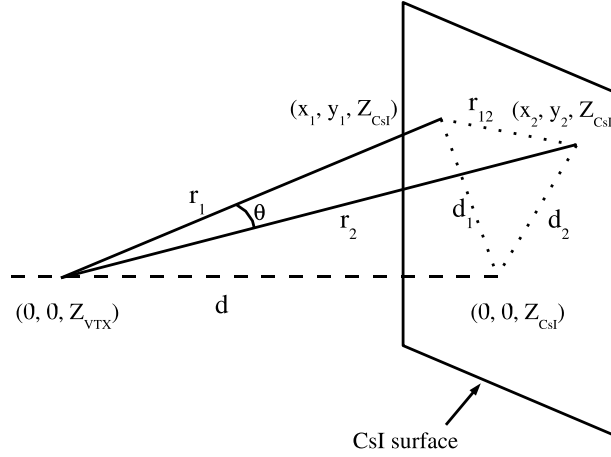
Figure 4.4: π^0 reconstruction

Decay vertex

Because of a narrow "pencil beam", the first step in reconstructing the decay vertex is assuming (x,y)=(0,0) as shown in Fig. 4.4. A pair of photons from each of the six "pairings" are taken to be decayed from the π^0, and the PDG value of 134.9766MeV used as its fixed mass. These conditions relate the opening angle θ and the measured energies E_1, E_2 to m_{π^0}:

$$\mathbf{p}_{\pi^0}^2 = (\mathbf{p}_1 + \mathbf{p}_2)^2$$
$$E_{\pi^0}^2 - m_{\pi^0}^2 = \mathbf{p}_1^2 + \mathbf{p}_2^2 + 2\mathbf{p}_1 \cdot \mathbf{p}_2$$
$$E_1^2 + E_2^2 + 2E_1E_2 - m_{\pi^0}^2 = E_1^2 + E_2^2 + 2E_1E_2\cos\theta$$
$$\cos\theta = 1 - \frac{m_{\pi^0}^2}{2E_1E_2}$$

with the opening angle defined, it is translated to the decay z vertex with the help of the following relations:

$$r_{12}^2 = r_1^2 + r_2^2 - 2r_1r_2\cos\theta$$
$$r_1 = \sqrt{d_1^2 + d^2}$$
$$r_2 = \sqrt{d_2^2 + d^2}$$

45

where d is just the distance between the z vertex and the CsI plane:

$$d = z_{CsI} - z_{VTX}$$

Once the decay z is found, we correct the decay x and y positions by asking the vertex to lie on the line connecting $(0, 0, z_{target})$ and $(x_{COE}, y_{COE}, z_{CsI})$, where "COE" means the center of energy of all four clusters combined. Or specifically:

$$x_{COE} = \frac{\sum_i E_i x_i}{\sum_i E_i}$$

where i counts the ith cluster.

$\underline{m_{\gamma\gamma}}$

The two "spare" photons, photon 3 and 4, which had been neglected in calculating z now have their invariant mass $m_{\gamma\gamma}$ calculated as:

$$
\begin{aligned}
E_{\gamma\gamma}^2 &= \mathbf{p}_{\gamma\gamma}^2 + m_{\gamma\gamma}^2 \\
(E_3 + E_4)^2 &= (\mathbf{p}_3 + \mathbf{p}_4)^2 + m_{\gamma\gamma}^2
\end{aligned}
$$

or,

$$m_{\gamma\gamma} = \sqrt{(E_3 + E_4)^2 - (\mathbf{p}_3 + \mathbf{p}_4)^2}$$

where

$$
\begin{aligned}
\mathbf{p}_3 &= \frac{E_3}{r_3} \times (x_3, y_3, d) \\
\mathbf{p}_4 &= \frac{E_4}{r_4} \times (x_4, y_4, d)
\end{aligned}
$$

are the momentum vectors derived from the decay vertex.

Constrained refit

After obtaining a decay vertex, a constrained refit is applied to optimize the decay vertex under kinematic constraints including K_L and π^0 masses, while the cluster energies and positions are varied. Finally a better decay vertex is obtained, and the $m_{\gamma\gamma}$ resolution is improved 35%. Details of the fitting method are given in Appendix B. A comparison of K_L, π^0 and $\gamma\gamma$ masses before and after the constrained fit is shown in Fig. 4.5.

46
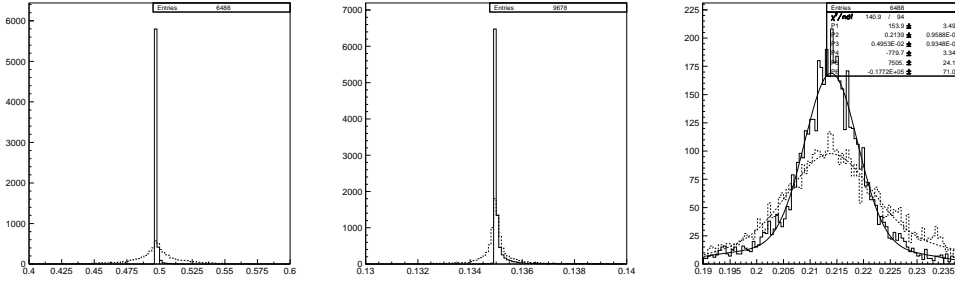
Figure 4.5: m_{K_L}, m_{π^0} and $m_{\gamma\gamma}$ (GeV, dashed: before fit, solid: after fit)

Refit χ^2

The refit χ^2 is a function of measured cluster positions and energies as well as fitted ones:

$$\chi^2 = \sum_i \left(\frac{\Delta x_i^2}{\sigma_x^2} + \frac{\Delta y_i^2}{\sigma_y^2} + \frac{\Delta E_i^2}{\sigma_E^2}\right) \tag{4.4}$$

where

$$
\begin{aligned}
\Delta x_i &= x_i^{fit} - x_i^{meas} \\
\Delta y_i &= y_i^{fit} - y_i^{meas} \\
\Delta E_i &= E_i^{fit} - E_i^{meas}
\end{aligned}
$$

In effect, this is an indicator to how much we modified the measured energies and positions of the clusters in order to meet the constraints. The six pairings are sorted by the χ^2 from small to large, which are then called "1st pairing/χ^2", "2nd pairing/χ^2" and so on. The 1st pairing, the pairing with the smallest χ^2, is assumed to be the correct pairing. Generally, the higher 2nd and 3rd χ^2s are, the more we are certain that the 1st pairing is correct. Fig. 4.6 illustrates the comparison of χ^2 between $K_L \to 2\pi^0$ and $K_L \to \pi^0 X$ for the first three pairings.

Energy and Angle Correction

Due to the CsI's limited length ($16X^0$), the electromagnetic shower can leak out from the crystal. Also, a photon incident at an angle generates a cluster center that's laterally displaced from the incident point as shown
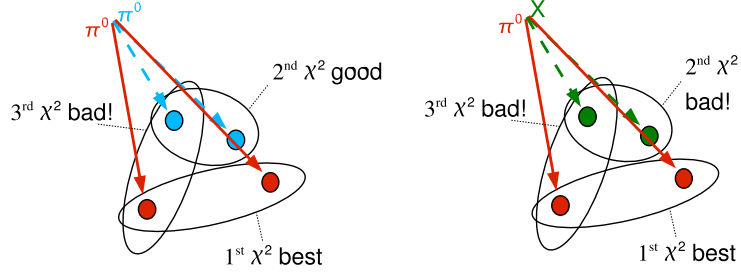
Figure 4.6: 1st, 2nd and 3rd χ^2's (left: $K_L \to 2\pi^0$, right: $K_L \to \pi^0 X$)

in Fig. 4.7. Thus, a shower leakage energy correction and a cluster angle correction [21] are applied to each cluster to reduce these effects.

The energy correction algorithm takes the vertex, fitted cluster energy and position as input, and follows a table obtained from a MC simulation to return an energy correction:

$$\Delta E = C_x \times \Delta E_x + C_y \times \Delta E_y + A\sqrt{C_x \times \Delta E_x \times C_y \times \Delta E_y} \qquad (4.5)$$

where
$$\begin{aligned} \Delta E_x &= table(E_x, \theta_x, x) \\ \Delta E_y &= table(E_y, \theta_y, y) \end{aligned} \qquad (4.6)$$

and
$$\begin{aligned} E_x &= E|cos\phi| & E_y &= E|sin\phi| \\ \theta_x &= tan^{-1}(|cos\phi||tan\theta|) & \theta_y &= tan^{-1}(|sin\phi||tan\theta|) \\ C_x &= |cos\phi| & C_y &= |sin\phi| \end{aligned} \qquad (4.7)$$

The parameter A is found to be 0.631741 by aligning the $E_{corr} - E_{in}$ dsitribution to peak at 0, as shown in Fig. 4.8.

The result of the energy correction as studied in MC is shown in Fig. 4.9.

The next step is the angle correction, which corrects the clusters' θ angles, or in other words, their radial positions. It is also a table-based algorithm
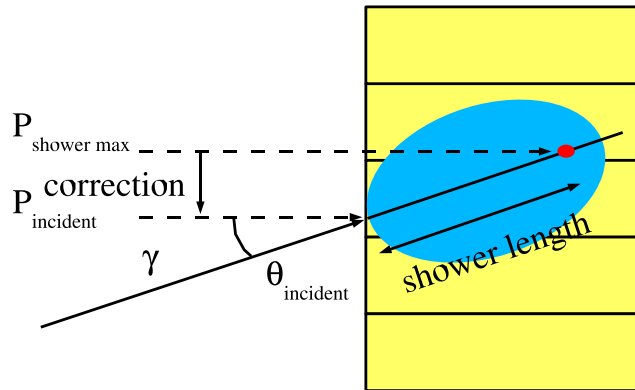
Figure 4.7: The difference in C.O.E. position and true γ incident position
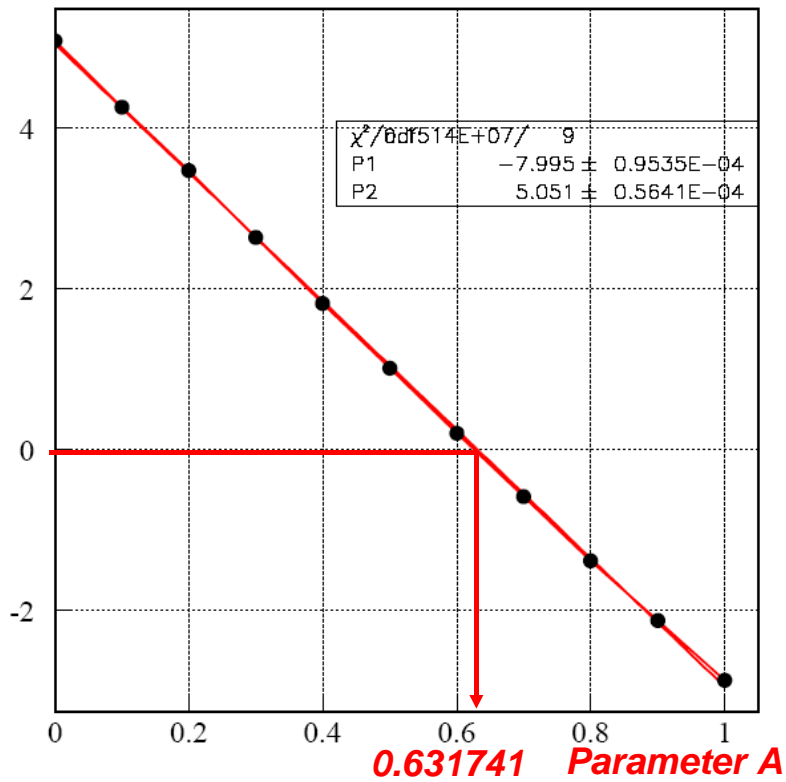
Figure 4.8: Peak position of $E_{corr} - E_{in}$ vs parameter A
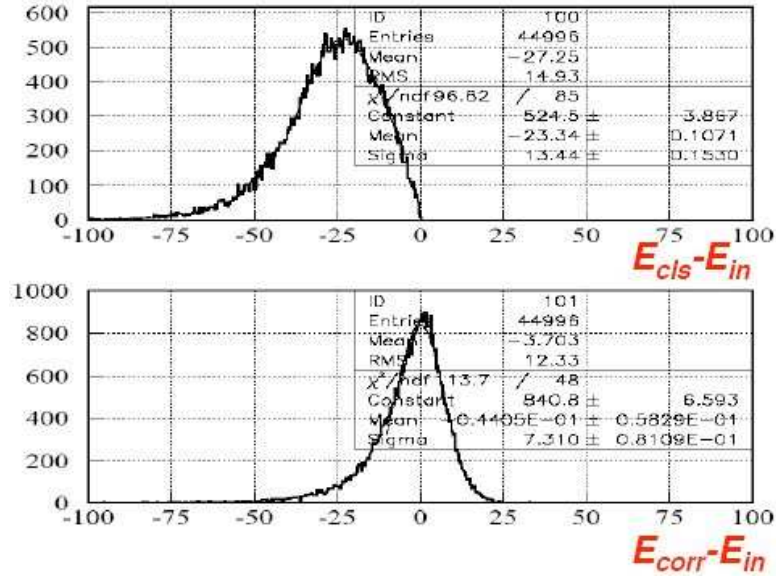
Figure 4.9: Result of the energy correction (upper: before, lower: after)

that takes decay vertex, cluster energies and positions as input and returns corrected cluster positions, where the table is obtained from a MC simulation:

$$
\begin{aligned}
x_{corrected} &= table(E_x, \theta_x, x_{original}) \\
y_{corrected} &= table(E_y, \theta_y, y_{original})
\end{aligned}
\tag{4.8}
$$

where

$$
\begin{aligned}
E_x &= E\cos\phi & E_y &= E\sin\phi \\
\theta_x &= tan^{-1}(|\cos\phi||\tan\theta|) & \theta_y &= tan^{-1}(|\sin\phi||\tan\theta|)
\end{aligned}
\tag{4.9}
$$

while ϕ and θ represent the direction of the incident photon, in the usual detector cylindrical coordinate. Results of this correction are shown in Fig. 4.10.

The refit χ^2 is improved slightly by incorporating the above energy and angle corrections. The comparison in χ^2 is shown in Fig. 4.11.

Iterations of correction

The process of constrained refit followed by energy and angle corrections is iterated as a whole. Each iteration, the refit χ^2 is compared to that of the previous iteration. In practice, fewer than 5 iterations are required to optimize the refit χ^2.
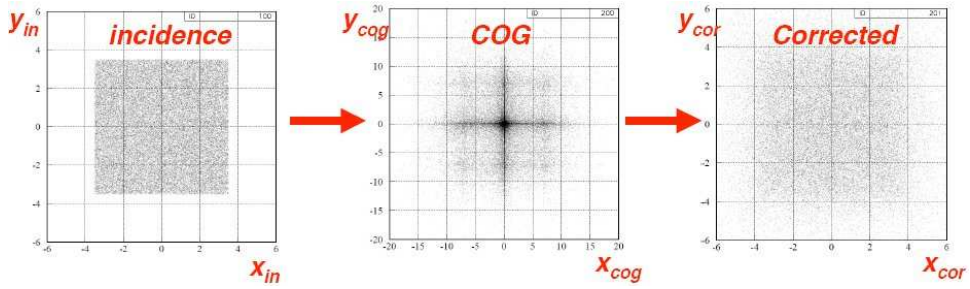
Figure 4.10: Result of the angle correction (left: generated, middle: before correction, right: after correction)
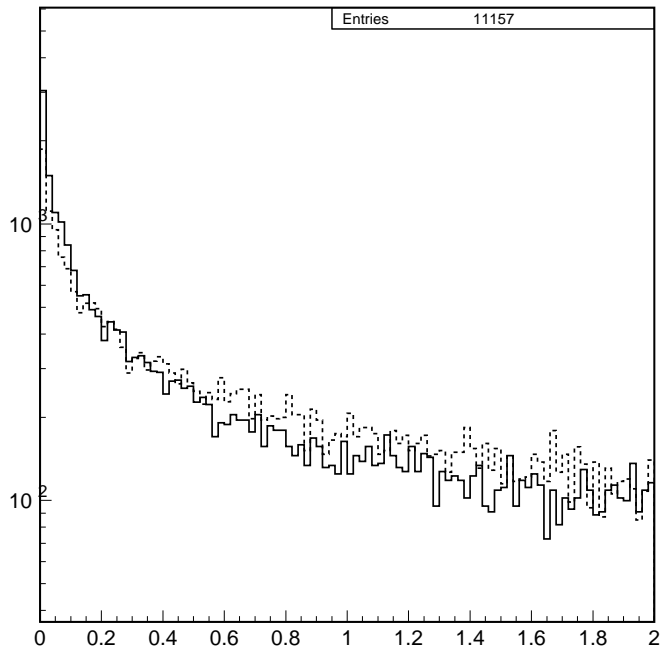
Figure 4.11: Refit χ^2 before (dashed) and after (solid) corrections
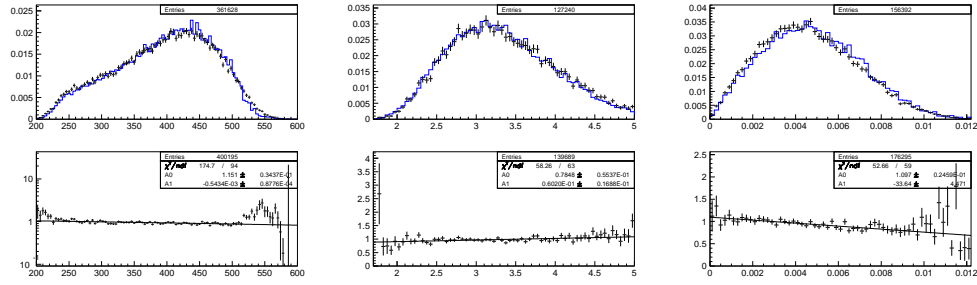
Figure 4.12: Kinematic variables, data (black) vs MC (blue) (left to right: z vertex (cm), K_L momentum(GeV), K_L transverse momentum (GeV))

4.2.3   Reconstruction results

The reconstructed kinematic variables show good agreement between data an MC, as shown in Fig. 4.12. The $m_{\gamma\gamma}$ mass peak (Fig. 4.13) shows a "dip" at 135 MeV, the mass of the π^0. This is entirely expected, and is due to the event reconstruction method: For all pairings, the 1st pair always takes the gamma pair with the reconstructed $m_{\gamma\gamma}$ closest to m_{π^0}. This makes for the lowest χ^2 when the kinematic refit is applied, constraining the 1st $m_{\gamma\gamma}$ to m_{π^0}. For $2\pi^0$ decays, this means the 2nd gamma pair, although decayed from a real π^0, always reconstructs to worse m_{π^0} than the 1st pair with or without refit. In effect, the π^0 mass peak in the $m_{\gamma\gamma}$ plot resembles a narrow Gaussian subtracted from a wider one.

4.3   Candidate Selection

For this decay mode, we require $N_{CLS} = 4$ due to both $\mathcal{B}(K_L \rightarrow 2\pi^0)$ and $\mathcal{B}(K_L \rightarrow \pi^0 X)$ ultimately decaying to 4 photons, when π^0 decays immediately to 2 photons and X assumed so. A signal event would be identified by a reconstructed $\gamma\gamma$ invariant mass ($m_{\gamma\gamma}$) at 214.3MeV while the other $m_{\gamma\gamma}$ is 134.9766MeV, mass of the π^0 (PDG, [8]).

4.3.1   Signal box

The signal is identified by $m_{\gamma\gamma}$ inside target mass regions, which are called signal boxes. The four contiguous signal boxes are centered around the four
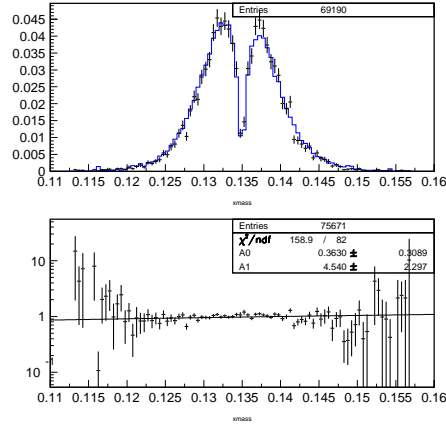
Figure 4.13: data (black) vs MC (blue), $m_{\gamma\gamma}$ in π^0 region (GeV)

target masses, and are about $\pm 2\sigma$ of the resolution obtained from signal MC. The signal boxes are used for both likelihood fitting and event counting. Details of the signal boxes are shown as below:

$X_{181.7}$:	$173.55 < m_{\gamma\gamma} < 189.85 (MeV)$
$X_{198.0}$:	$189.85 < m_{\gamma\gamma} < 206.15 (MeV)$
$X_{214.3}$:	$206.15 < m_{\gamma\gamma} < 222.45 (MeV)$
$X_{230.6}$:	$222.45 < m_{\gamma\gamma} < 238.75 (MeV)$

4.3.2 π^0 region

There is an additional mass region for $m_{\gamma\gamma}$ that contains the π^0 mass, which is called the π^0 region. The π^0 region is centered on π^0 mass of 135MeV, and spans about $\pm 4\sigma$ of the π^0 mass peak. The π^0 region is used for counting the number of $K_L \to 2\pi^0$ decays as event normalization. For all purposes, the π^0 region is defined as:

$$112.95 < m_{\gamma\gamma} < 157.01 (MeV)$$

4.4 Background Suppression

The dominant background for this mode is the neutral decay $K_L \to 3\pi^0$ with 6 final photons where 2 of the photons are missing, resulting in 4 clusters

on the CsI grid. It is suppressed by a combination of tight veto cuts, event reconstruction quality and decay kinematics. Also, if a pair of photons hit the CsI close to the same spot, their showers can merge into a single cluster. This is called a fusion cluster. If there were 1 such fusion cluster and a missing photon, or 2 fusion clusters, we'd have $N_{CLS} = 4$, which can contribute to background. This is suppressed by cluster quality cuts.

Another background comes from the decay $K_L \rightarrow \pi^0 \gamma\gamma$, which also has 4 photons as final products. This mode with a branching ratio $(1.49 \pm 0.08) \times 10^{-6}$ is comparable to $K_L \rightarrow \pi^0 X$, but has an $m_{\gamma\gamma}$ spectrum spread throughout the kinematically allowed range, so it is not specifically suppressed.

$K_L \rightarrow 2\pi^0$ can leave a tail on the $m_{\gamma\gamma}$ spectrum due to wrong pairing of photons during event reconstruction. This can be almost eliminated by reconstruction quality cuts.

The neutrons that remain in the beam can interact with detector materials and generate "fake" π^0's that did not decay from a K_L, in the process similar to (2.2). This kind of background is "simulated" in the MC by the accidental overlay method as decribed in section 3.5. However, it is not likely to generate four photons and survive the other selection cuts so this background is not specifically suppressed.

4.4.1   Veto cuts

In order to reject events with missing photons, all veto detectors are used and thresholds for energy deposits applied. The veto cut points are taken from a "Run2 Common Cuts" set of thresholds used in the $\pi^0 \nu\bar{\nu}$ analysis. They are listed in Table 4.1. Fig. 4.14 shows energy distributions for each veto detector with all other veto cuts applied. Note that the MB cut points, due to a high correlation to decay vertex position, are optimized after some kinematic cuts. The Common Cuts are not applied to the MB.

CsI veto

The CsI veto is a set of conditions that reject events with single crystal energies which do not develop into clusters. It consists of single crystal energy, E_{single} (GeV), and the distance from the single crystal to the nearest cluster, d_{min} (cm). It is defined to be 1 when:
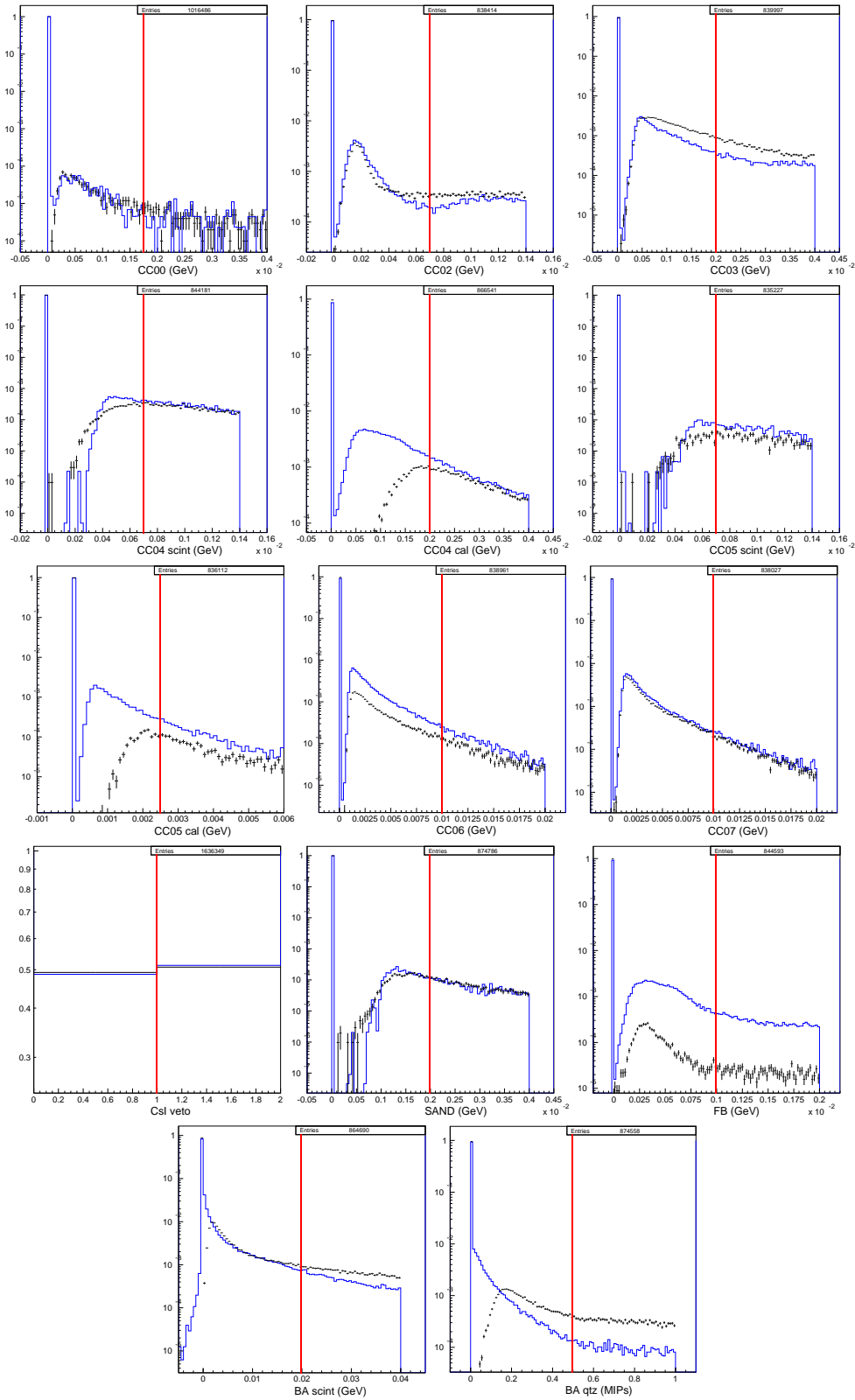
Figure 4.14: "Exclusive" veto energy distributions. Cut points are exactly middle points in all plotted ranges. (black: data, blue: MC)

Table 4.1: Run2 Common Cuts (MeV)

CC00	FB	CC02	BCV	Inner MB
2	1	1	0.75	1

Outer MB	Inner CV	Outer CV	CC03	CsI
1	0.7	0.3	2	see <u>CsI veto</u>

SAND	CC04 scint	CC04 cal	CC05 scint	CC05 cal
2	0.7	2	0.7	3

CC06	CC07	BHCV	BA scint	BA Qtz
10	10	0.1	20	0.5(MIPs)

$$d_{min} < 17 \quad AND \quad E_{single} > 0.01$$
$$17 < d_{min} < 25 \quad AND \quad E_{single} > 0.005 - (0.003/8)(d_{min} - 17)$$
$$25 < d_{min} < 35 \quad AND \quad E_{single} > 0.002$$
$$35 < d_{min} \quad AND \quad E_{single} > 0.0015$$

and 0 otherwise.

<u>Back Anti</u>

The BA cut uses a unique "AND" structure to combine the scintillator part (scint) and the quartz part (Qtz), which means an event is only rejected if both the scintillator AND the quartz record energies above their thresholds. This helps discriminate between neutrons and photons as mentioned in section 2.3.6.

Also, the sum of all channels are used for the scintillator part, while only the max reading from the quartz part is used.

4.4.2   Kinematic and MB cuts

I follow a structured approach to optimize kinematic selection cuts, the stages shown in Fig. 4.15. This optimization is targeted at suppressing background decays in the signal boxes while retaining signal efficiency. Due to a clear

Signal Boxes for $m\gamma\gamma$ (MeV)
$X_{181.7}$: 173.55 ~ 189.85
$X_{198.0}$: 189.85 ~ 206.15   →z-vertex →
$X_{214.3}$: 206.15 ~ 222.45
$X_{230.6}$: 222.45 ~ 238.75

Kinematics+MB
P_T
Refit χ^2
Inner MB->Outer MB

Cluster Fusion
gamma1 RMS
gamma2 RMS
gamma3 RMS
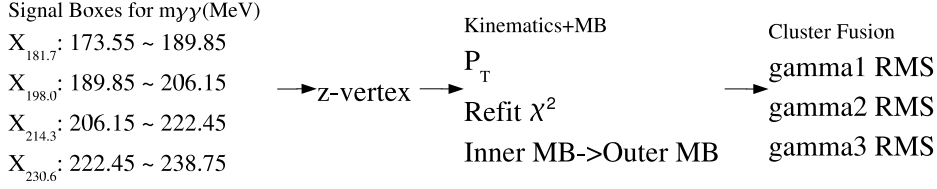
Figure 4.15: Structured approach to background suppression

dominant background mode of $K_L \to 3\pi^0$, the background study is best proceeded by comparing signal MC and $3\pi^0$ MC. For each variable, the significance was calculated over a range of cut points as a figure of merit. The significance is defined as:

$$significance = \frac{N_{signal,expected}}{\sqrt{N_{signal,expected} + N_{background,expected}}} \quad (4.10)$$

In order to "expect" $N_{signal,expected}$ for the calculation of the significance, a reference branching ratio for the decay $K_L \to \pi^0 X$ is taken to be:

$$
\begin{aligned}
\frac{\mathcal{B}(K_L \to \pi^0 X)}{\mathcal{B}(K_L \to 2\pi^0)} &\simeq \frac{\mathcal{B}(K_L \to \pi^0\pi^0 X)}{\mathcal{B}(K_L \to 3\pi^0)} \\
\Rightarrow \mathcal{B}(K_L \to \pi^0 X) &\simeq \mathcal{B}(K_L \to 2\pi^0) \times \frac{\mathcal{B}(K_L \to \pi^0\pi^0 X)}{\mathcal{B}(K_L \to 3\pi^0)} \\
&\simeq 5.33 \times 10^{-7}
\end{aligned}
$$

This reference "branching ratio" is used for the sole purpose of optimizing cuts through significance. However, it is found that the significance function is so dominated by effects from $N_{background,expected}$, that this "branching ratio" could be 10 times greater or smaller and the chosen cut points would not be changed.

Decay Z-vertex

The reconstructed decay z-vertex is very powerful at discriminating signal from background. Due to the fact that $3\pi^0$ decays would require two photons missing to satisfy $N_{CLS} = 4$, energy deposits on the CsI is only a fraction of the total energy. Furthermore, during reconstruction the K_L mass is held constrained. In order to satisfy the K_L mass constraint with missing energy, the reconstructed z-vertex will shift downstream from the true vertex to compensate.
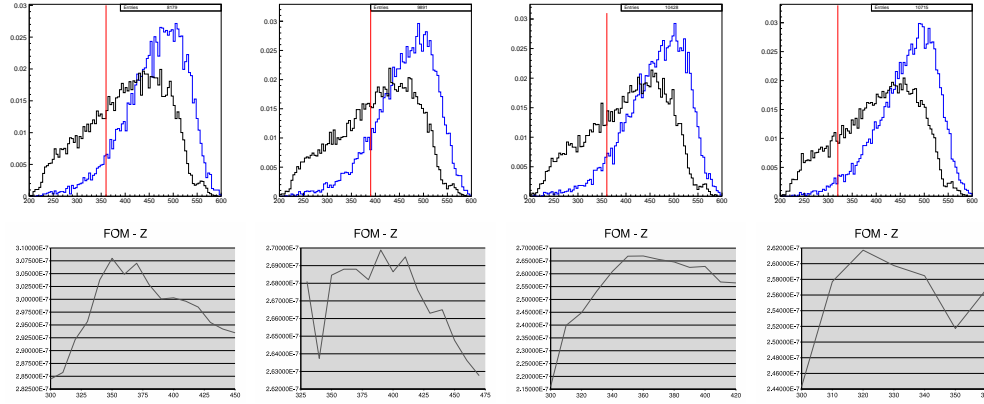
Figure 4.16: Decay z-vertex range for $X_{181.7}$, $X_{198.0}$, $X_{214.3}$ and $X_{230.6}$ (cm, blue: $3\pi^0$ MC, black: signal MC)
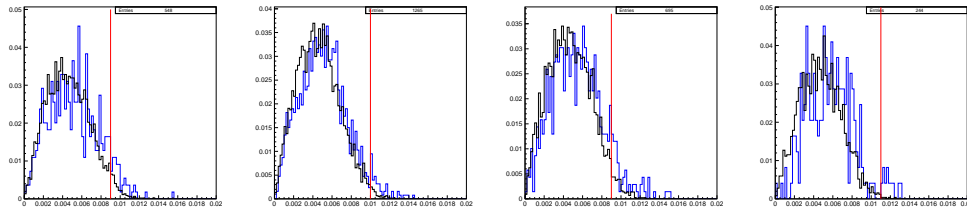
Figure 4.17: K_L transverse momentum (GeV)

As shown in Fig. 4.16, a cut is imposed on the z-vertex, and only upstream events are selected.

Note: Beginning from this stage, analyses for $X_{181.7}$, $X_{198.0}$, $X_{214.3}$ and $X_{230.6}$ proceed in parallel. Plots shown four abreast will stand for the four analyses without specifying. Also blue color always stands for the background mode in overlays.

K_L transverse momentum

Thanks to a well collimated beam, the K_L's transverse momentum is small coming into the detector. However, a missing photon usually carries away transverse momentum so a low reconstructed transverse momentum is desired, indicating no missing photons. The cut points are shown in Fig. 4.17.

Inner and Outer MB

58
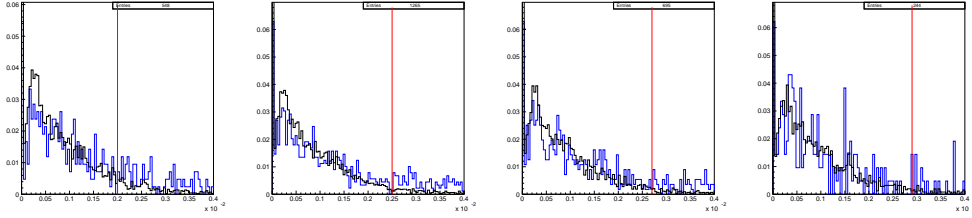
Figure 4.18: Inner MB (GeV)
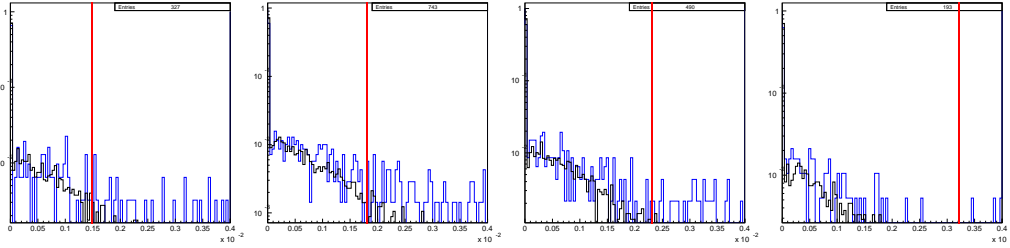
Figure 4.19: Outer MB (GeV, y in log scale)

The MB catches missing photons. Due to the very upstream decay region used, however, it is cut looser than the Common Cuts. Inner MB cuts are shown in Fig. 4.18, and Outer MB cuts are shown in Fig. 4.19.

Refit χ^2

The 1st refit χ^2 indicates the quality of the event reconstruction. A cut is applied to reject events with wrong cluster energies or $K_L \rightarrow 3\pi^0$ decays with missing photons. Shown in Fig. 4.20.
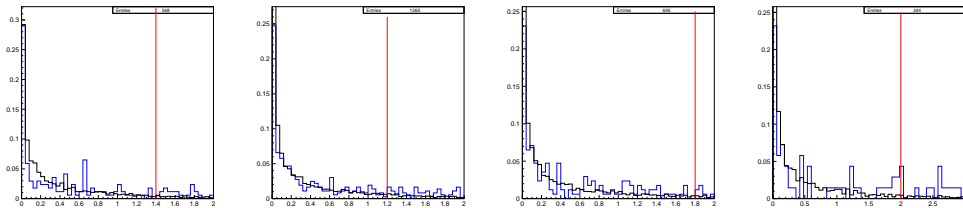
Figure 4.20: 1st refit χ^2

4.4.3 Cluster quality

If a $K_L \rightarrow 3\pi^0$ decay has one photon missing and two others fused into a single cluster, or if four photons are fused into two clusters, the event will be well reconstructed and not strongly suppressed by other selection cuts. To reject this kind of fusion clusters, a cluster property called "gamma RMS" is brought to use.

The gamma RMS is defined as:

$$RMS = \sqrt{\frac{\sum_i E_i r_i^2}{\sum_i E_i}} \tag{4.11}$$

where E_i is the energy of the ith crystal in a cluster, and r_i is the ith crystal's distance to the center of that cluster. It is a measure of how much the cluster energy is spread out, which we would expect from a cluster formed by two photons in proximity.

Internally, clusters are sorted by energy from high to low. If a cluster is a fusion cluster by nature, then it'll likely have the higher energy of two photons combined. This means the RMS cut should be more powerful on cluster 1, while nearly useless on cluster 4. As found by the FOM method, RMS 1 is generally cut tighter acceptance-wise, and RMS 4 is not used.

The FOM method, due to very low MC statistics after all previous cuts, requires extra caution to avoid bias. When statistics are low, a slightly tighter cut point removing just one more background event can result in a high peak in significance. However, if the cut point is chosen at this peak in significance, the number of background will most likely be underestimated, introducing a bias. This problem is worked around by choosing the three highest peaks, then taking their average weighted by respective significances. Cut points and FOM curves are shown in Fig. 4.21, Fig. 4.22 and Fig. 4.23. Events with high RMS clusters are rejected.

The gamma RMS cuts are found to be highly effective at suppressing $3\pi^0$ events across all the signal box regions, removing 84% of the background while retaining 86% of the signal, as shown in Fig. 4.24. However, tightening the cut anymore will remove both signal and background events indiscriminately.
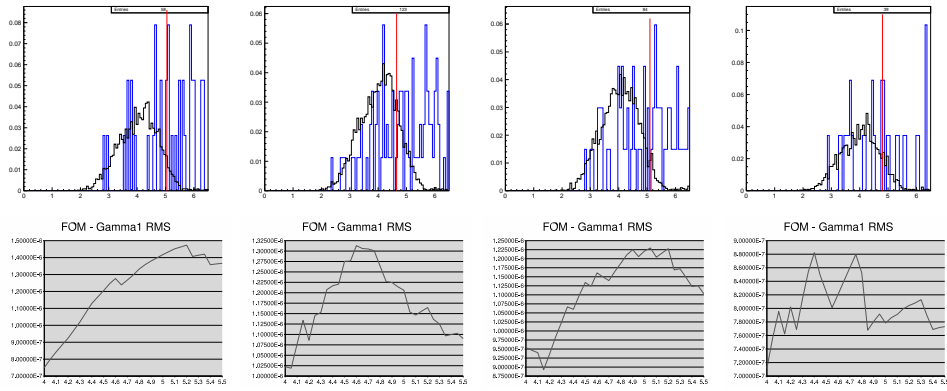
Figure 4.21: Gamma RMS 1 (cm)
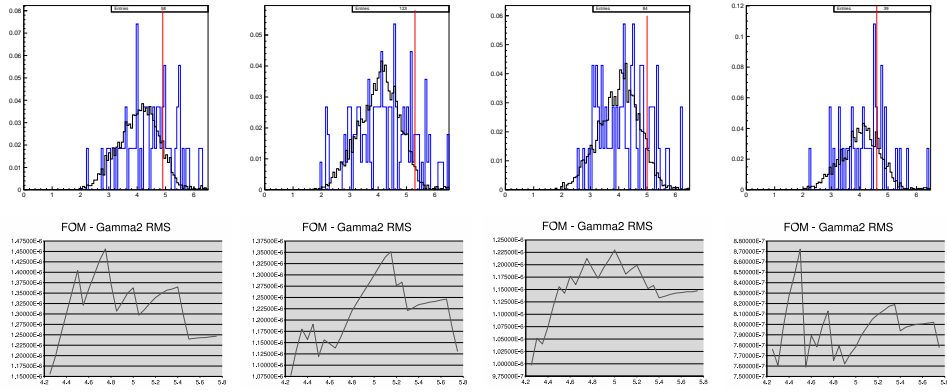
Figure 4.22: Gamma RMS 2 (cm)
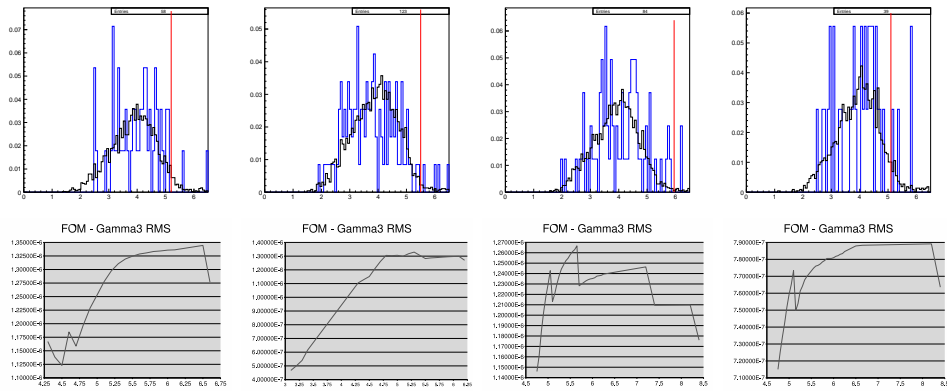
Figure 4.23: Gamma RMS 3 (cm)

61
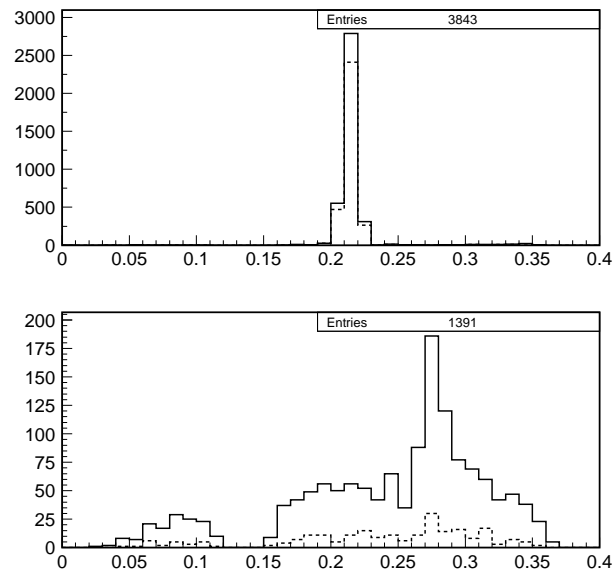
Figure 4.24: $m_{\gamma\gamma}$ before (solid) vs after (dashed) RMS cuts (upper: signal MC, lower: $3\pi^0$ MC)
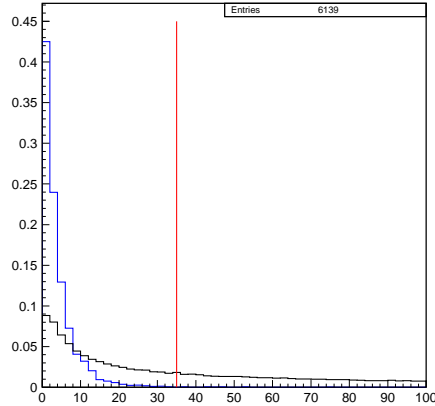
Figure 4.25: 3rd χ^2 from $2\pi^0$ MC (blue: outside π^0 region, black: inside π^0 region)

4.4.4 π^0 tail

In the reconstruction of $K_L \rightarrow 2\pi^0$ events, sometimes the correct pairing remains ambiguous up to the 3rd pairing, where only 2 pairings can possibly be correct. This kind of combinatorial background is suppressed by requiring the 3rd χ^2 to be bad, but leaving the 2nd χ^2 untouched. This criterion saves both $K_L \rightarrow 2\pi^0$ and $K_L \rightarrow \pi^0 X$ events, as illustrated in Fig. 4.6.

Only events with 3rd $\chi^2 > 35$ are selected as shown in Fig. 4.25.

4.4.5 K_L radius at the exit of collimator 6

This kinematic cut comes from the Common Cuts. From the reconstructed vertex, the K_L's radius at C6 is obtained by tracing the K_L trajectory back to the (assumed) point production target and finding the radius as it leaves C6. The cut point is set at $R^2_{C6} < 4.5 cm^2$, as shown in Fig. 4.26. This should remove K_L's that have reconstructed trajectories cutting through C6 which has a 2.2cm radius.

4.4.6 Selection results

The background distribution after event selection is shown in Fig. 4.27, while the final acceptances in signal boxes are listed below:
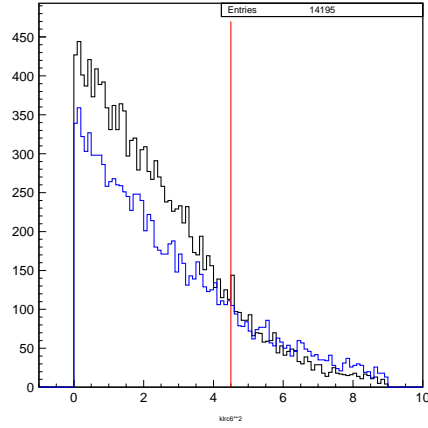
Figure 4.26: R_{C6}^2 of the K_L (cm^2, blue: $3\pi^0$ MC, black: signal MC)
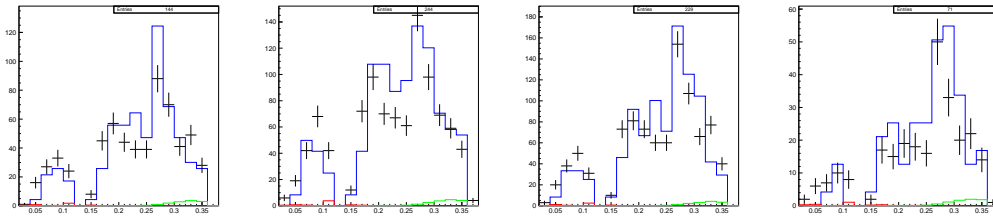
Figure 4.27: $m_{\gamma\gamma}$, excluding π^0 region (GeV, black: data, blue: $3\pi^0$, green: $\pi^0\gamma\gamma$, red: $2\pi^0$)

	$X_{181.7}$	$X_{198.0}$	$X_{214.3}$	$X_{230.6}$
$2\pi^0$	0	0	0	0
$3\pi^0$ $(\times 10^{-10})$	7.00 ± 2.65	19.0 ± 4.36	15.0 ± 3.87	6.00 ± 2.45
$\pi^0\gamma\gamma$ $(\times 10^{-7})$	3.87 ± 0.72	3.60 ± 0.69	5.20 ± 0.83	1.73 ± 0.48
signal $(\times 10^{-5})$	3.22 ± 0.07	4.42 ± 0.08	3.90 ± 0.07	1.90 ± 0.05

Chapter 5

Signal Extraction

5.1 Likelihood Method

The maximum likelihood method is used for signal extraction. It is superior to a simple counting method in that the signal and background distributions are taken into account in the form of Probability Density Functions (PDF's), instead of only event counts.

In this analysis, the maximum likelihood method is applied to the $m_{\gamma\gamma}$ distribution for signal extraction. Some parameters in signal and background distributions are fixed with information from MC samples. For all the fixed parameters in the PDF's, systematic errors are investigated in section 5.2.1.

5.1.1 Definition

Likelihood is defined as:

$$\mathcal{L} = \frac{e^{-(N_S+N_B)}}{N!} \prod_i (N_S \times P_S(m_i) + N_B \times P_B(m_i)) \tag{5.1}$$

It is a measure of how "likely" the hypothesis (N_S and N_B) will be, given the measurements (m_i). This is opposed to the measure of how "probable" we are to obtain the measurements, given the hypothesis. The maximum likelihood method maximizes this value to determine the most likely hypothesis.

In practice, we instead *minimize* the value $-2\log\mathcal{L}$ with respect to its variables (N_S and N_B in this case). This allows us to reach the maximum likelihood, while at the same time obtain errors on the corresponding variables. Because $-2\log\mathcal{L}$ itself is a χ^2-like value, and exactly so when $\mathcal{L}$ approaches Gaussian, Δu would be quoted as (Gaussian) error on value u_{MAX}
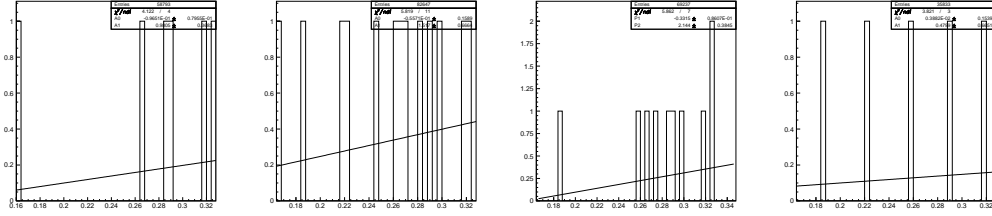
Figure 5.1: $K_L \to 2\pi^0$ PDF ($m_{\gamma\gamma}$, GeV)

if $-2\log\mathcal{L}(u_{MAX} + \Delta u) - (-2)\log\mathcal{L}(u_{MAX}) = 1$. This error is used to determine if we have significant signals from the fit results.

5.1.2 Background PDF

For the three background modes considered, $K_L \to 2\pi^0$, $K_L \to 3\pi^0$ and $K_L \to \pi^0\gamma\gamma$, their respective PDF's are obtained from each MC sample. We only obtain the function shape for each mode here. Normalization of the total background PDF comes after these non-normalized PDF's are combined.

$\underline{K_L \to 2\pi^0}$

The $2\pi^0$ background is the weakest, and none enters the signal boxes. However, some events are scattered about which may imply some contamination. This background is given a straight-line fit which extended into the signal boxes, as shown in Fig. 5.1.

Fitted parameters for $f(m) = A + B \cdot m$ (m in GeV):

	$X_{181.7}$	$X_{198.0}$	$X_{214.3}$	$X_{230.6}$
A	-0.097	-0.056	-0.331	0.004
B	0.981	1.517	2.144	0.480

$\underline{K_L \to 3\pi^0}$

The $3\pi^0$ background, although being the main target of background suppression, is still dominant with over 99% contribution. As shown in Fig 5.2, its distribution is modelled by a straight-line for the continuum part, and a Gaussian peak for the residual double fusion cluster events near 270 MeV. The low statistics of available MC is apparent here, which denies us a better modelling of the continuum part.

67
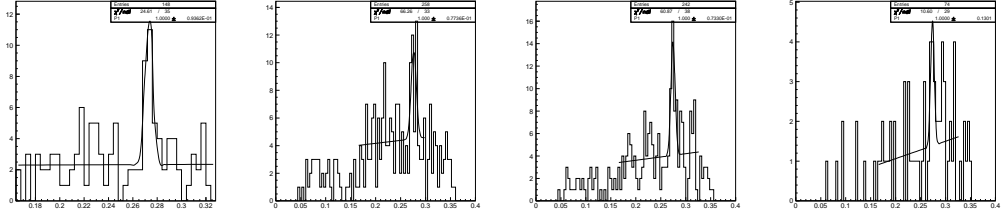
Figure 5.2: $K_L \to 3\pi^0$ PDF ($m_{\gamma\gamma}$, GeV)
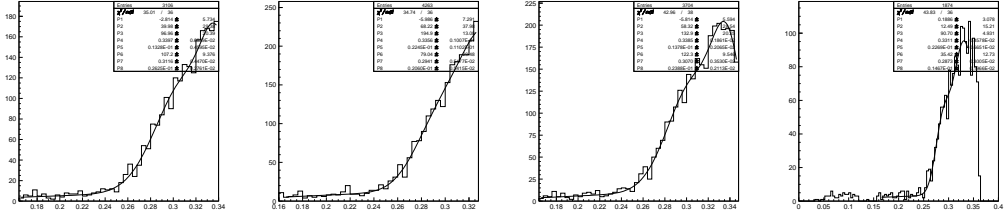
Figure 5.3: $K_L \to \pi^0\gamma\gamma$ PDF ($m_{\gamma\gamma}$, GeV)

Fitted parameters for $f(m) = A + Bm + Gaussian(m; norm, mean, \sigma)$:

	$X_{181.7}$	$X_{198.0}$	$X_{214.3}$	$X_{230.6}$
A	9.402	16.94	15.09	4.879
B	0.033	0.251	0.390	0.900
$norm$	0.074	0.083	0.106	0.029
$mean$	0.273	0.276	0.275	0.274
σ	0.003	0.005	0.001	0.004

$K_L \to \pi^0\gamma\gamma$

The $K_L \to \pi^0\gamma\gamma$ mode is very well simulated, along with statistics 240 times more than that of data equivalent. The PDF is obtained by fitting with a straight-line plus two Gaussians, as shown in Fig. 5.3. The original generating function was not used due to a non-uniform efficiency over the mass region.

Fitted parameters for
$$f(m) = A + Bm + Gaussian(m; norm_1, mean_1, \sigma_1) + Gaussian(m; norm_2, mean_2, \sigma_2):$$

68

	$X_{181.7}$	$X_{198.0}$	$X_{214.3}$	$X_{230.6}$
A	-2.814	-5.986	-5.814	0.189
B	39.98	68.22	58.32	12.49
$norm_1$	96.91	194.9	132.9	90.70
$mean_1$	0.340	0.336	0.338	0.331
σ_1	0.013	0.023	0.014	0.023
$norm_2$	107.2	79.04	122.4	35.42
$mean_2$	0.312	0.294	0.307	0.287
σ_2	0.026	0.021	0.024	0.015

5.1.3 Background normalization

By normalizing backgrounds to data, we follow a fixed background approach for the final fit because a) The large number of surviving $K_L \rightarrow 2\pi^0$ events allows for precise normalization to data, b) The low statistics for the data around the signal boxes hinder proper fitting for floating background PDF's, and c) The lesser background modes $K_L \rightarrow 2\pi^0$ and $K_L \rightarrow \pi^0\gamma\gamma$ are drown out by the dominant mode of $K_L \rightarrow 3\pi^0$ around the signal boxes (see Fig. 4.27) so their relative scales cannot be obtained from the fit, but must be fixed instead.

The number of events from data falling into the π^0 region *almost* represents the actual amount of $K_L \rightarrow 2\pi^0$ decays. However, the MC samples still show a very low level contamination of $K_L \rightarrow 3\pi^0$ and $K_L \rightarrow \pi^0\gamma\gamma$ events. The number of $2\pi^0$ events is thus corrected by:

$$N_{2\pi^0}^{data} = N_{\pi^0 region}^{data} \times (\frac{N_{\pi^0 region}^{2\pi^0}}{N_{\pi^0 region}^{2\pi^0} + N_{\pi^0 region}^{3\pi^0} + N_{\pi^0 region}^{\pi^0\gamma\gamma}})^{MC} \qquad (5.2)$$

The corrected numbers are shown as follows:

	$X_{181.7}$	$X_{198.0}$	$X_{214.3}$	$X_{230.6}$
observed	$5617 \pm \sqrt{5617}$	$7666 \pm \sqrt{7666}$	$6481 \pm \sqrt{6481}$	$4185 \pm \sqrt{4185}$
corrected	5599.7 ± 82.0	7607.8 ± 95.8	6426.6 ± 88.2	4163.7 ± 70.8
$2\pi^0$ MC	58747	82590	69165	44448
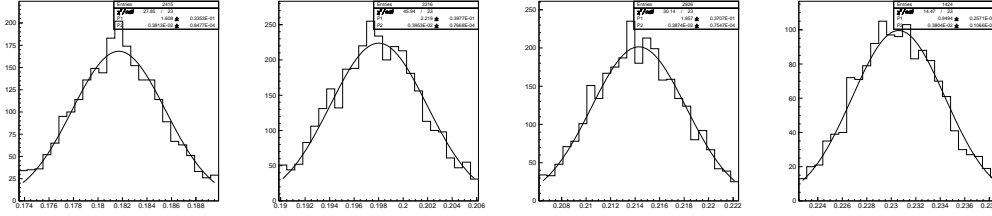
Figure 5.4: $K_L \to \pi^0 X$ PDF ($m_{\gamma\gamma}$, GeV)

5.1.4 Signal PDF

Signal PDF is obtained by fitting a Gaussian distribution on the signal MC as shown in Fig. 5.4. This is made possible because the signal MC is generated at a single m_X instead of a resonance distribution. The Gaussian *mean*s are fixed to be the generating masses of 181.7, 198.0, 214.3 and 230.6 MeV respectively. The σ's, on the other hand, are allowed to float here, but fixed later in signal extraction. We list the σ's as follows:

	$X_{181.7}$	$X_{198.0}$	$X_{214.3}$	$X_{230.6}$
σ(MeV)	3.81	3.95	3.87	3.80

5.1.5 Fit results

The fitting at this stage gives central values for N_S as (with corresponding N_B):

	$X_{181.7}$	$X_{198.0}$	$X_{214.3}$	$X_{230.6}$
N_S	1.02 ± 5.61	4.32 ± 7.76	-0.51 ± 6.92	-6.42 ± 2.80
N_B(fixed)	40.45	70.52	63.32	20.68
N_{total}^{obs}	39	77	59	11

where N_{total}^{obs} means the total observed event count in the signal boxes. There is no significant physical signal observed outside error, so upper limits to the N_S are set instead. The final values and upper limits for N_S will be obtained once systematic errors are considered for the likelihood function, in section 4.6.

5.2   Upper Limit Estimation

The upper limit is calculated using the likelihood function at 90% confidence level. This means the integrated likelihood from the physical lower limit of $N_S = 0$ to the upper limit N_S should cover 90% of the area of all physical N_S, i.e. $[0, \infty]$. Or,

$$\int_0^{upperlimit} \mathcal{L} dN_S = 0.9 \times \int_0^\infty \mathcal{L} dN_S \tag{5.3}$$

The likelihood function will need to incorporate the effect of systematic errors before this is applied, which is described as follows.

5.2.1   Systematic error study

For all the assumptions made in the fitting, the uncertainties in modelling and possible differences between data and MC could introduce systematic errors.

   In this part of the analysis, the parameters fixed from the MC study are varied, and the effects on their variations are translated into differences (ΔN_S) in the fitted number of signal (N_S). The uncertainties in the single event sensitivity is also included and considered as a percentage error on N_S. The sources of systematic errors are described in detail below.

$K_L \to 2\pi^0$ background

   The background coming from $K_L \to 2\pi^0$ background is modeled as shown in Fig. 5.1. Due to its very low contribution as shown in Fig. 4.27, the modelling error was estimated by "turning off" this background source and obtaining a new fitted N_S. The difference between fitted N_S and the original N_S, or ΔN_S, is quoted as the associated error.

$K_L \to 3\pi^0$ background

   This is the dominant background as shown in Fig. 4.27. The fluctuations in mass spectrum due to insufficient MC statistics limited PDF construction to only a straight line plus Gaussian. To gain an understanding in the modelling uncertainties, a different PDF is tried and the effect on N_S estimated.

   A PDF constructed from a parabolic and a Gaussian is fitted to the MC, as shown in Fig. 5.5. Then the new PDF along with its estimated N_B is used in the likelihood fit. The ΔN_S is quoted as the associated error.
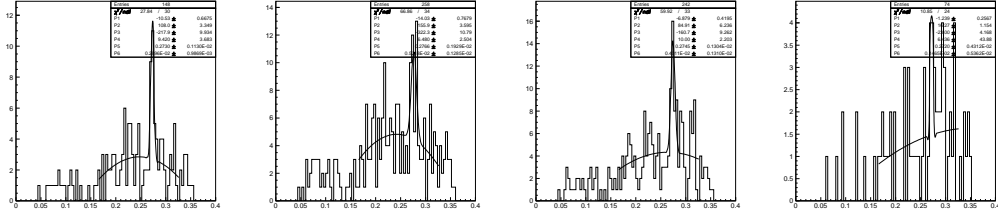
Figure 5.5: parabola+Gaussian alternate $3\pi^0$ PDF ($m_{\gamma\gamma}$, GeV)

Fitted parameters for
$$f(m) = A + Bm + Cm^2 + Gaussian(m; norm, mean, \sigma):$$

	$X_{181.7}$	$X_{198.0}$	$X_{214.3}$	$X_{230.6}$
A	-10.53	-14.03	-6.879	-1.240
B	108.0	155.9	84.91	16.27
C	-217.9	-322.3	-160.7	-23.00
$norm$	9.421	6.480	10.00	6.4358
$mean$	0.273	0.277	0.275	0.272
σ	0.003	0.005	0.004	0.001

Also, the scaling of this background mode has a great effect on the fitted N_S. The error in scaling comes from fitting error in obtaining the PDF. The error in scale is estimated by fitting the PDF to the MC sample, but holding all parameters fixed except for the overall scale, and obtaining the error on the overall scale. Errors in PDF scaling is around 10% as shown below:

	$X_{181.7}$	$X_{198.0}$	$X_{214.3}$	$X_{230.6}$
$\Delta scale$	9.36%	7.74%	7.33%	13.01%

To estimate the associated error in N_S, the fixed PDF scale in likelihood fitting is varied by this error in scale, and the resultant ΔN_S quoted as the systematic error.

$K_L \to \pi^0 \gamma\gamma$ background

Similar to the $K_L \to 2\pi^0$ background, the contribution is relatively low, and the error is obtained by "turning off" this mode and fitting again.

Mass resolution
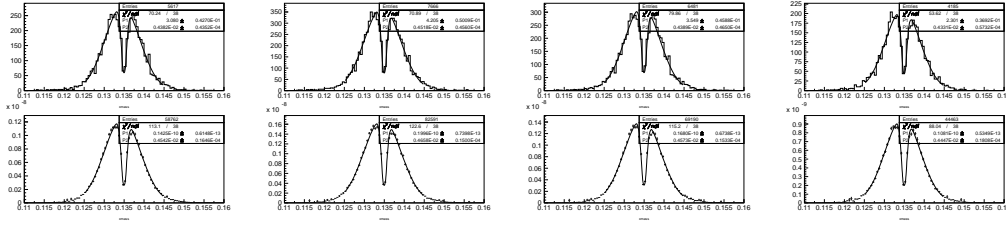
Figure 5.6: Double Gaussian fitted to the π^0 mass peak (GeV, upper: data, lower: MC)

The reconstructed $m_{\gamma\gamma}$ resolution is taken from MC study and is fixed for the signal PDF. The possible differences between data and MC can make this a source of systematic error. It is estimated by comparing the π^0 mass peak for data and MC.

Due to the "double peak" nature of the π^0 mass discussed in section 4.2.3, its mass spectrum is fitted by two added Gaussians. Gaussian A has a floating mean and positive norm. Gaussian B has a mean fixed at m_{π^0} of 134.9766 (MeV) and a negative norm, corresponding to the part taken away by the 1st photon pair. A+B is fitted to the MC, and then both their means, ratio of norms and ratio of σ's are fixed, leaving one σ and one norm as floating parameters. However we're only interested in the fitted σ's so the norms are meaningless here. This partially fixed double Gaussian is used to fit both the data and MC, and the ratio of the fitted σ's taken to be the ratio in resolution of data and MC. The fitting plots are shown as Fig. 5.6.

Fitted parameters for
$$f(m) = Gaussian_A(m; norm_A, mean_A, \sigma_A) + Gaussian_B(m; norm_B, mean_B, \sigma_B):$$

	$X_{181.7}$	$X_{198.0}$	$X_{214.3}$	$X_{230.6}$
fixed parameters				
$norm_B/norm_A$	-0.118	-0.115	-0.120	-0.122
σ_B/σ_A	0.146	0.142	0.149	0.150
$mean_A$	0.1346	0.1345	0.1346	0.1346
$mean_B$	m_{π^0}	m_{π^0}	m_{π^0}	m_{π^0}
floating parameters (data)				
$\sigma_{A,data}$	0.00438	0.00452	0.00439	0.00433
$\sigma_{A,MC}$	0.00454	0.00466	0.00457	0.00445
$\sigma_{A,data}/\sigma_{A,MC}$	96.5%	97.0%	96.0%	97.4%

The error it causes in ΔN_S is considered as a percentage error to N_S because its magnitude varies in proportion to N_S.

Single event sensitivity

Here, we rearrange (4.2) to better identify the errors caused by uncertainties in S.E.S. and normalizing in general.

$$\mathcal{B}(K_L \to \pi^0 X) \;\; = \;\; N_S \times \frac{A_{2\pi^0}}{N_{2\pi^0}^{obs} \times A_S} \times \mathcal{B}(K_L \to 2\pi^0) \qquad (5.4)$$

$$= \;\; N_S \times S.E.S. \qquad (5.5)$$

where A_S and $A_{2\pi^0}$ are acceptances of signal and $2\pi^0$ events respectively, which come from MC studies. And $N_{2\pi^0}^{obs}$ is the number of observed (corrected) $2\pi^0$ events from the data, as listed in section 5.1.3. The last term, $\mathcal{B}(K_L \to 2\pi^0)$, simply takes the PDG value of $(8.69 \pm 0.04) \times 10^{-4}$.

The acceptances for any *mode* and their errors are calculated from:

$$A_{mode} = \frac{N_{mode}^{accepted} \pm \sqrt{N_{mode}^{accepted}}}{N_{mode}^{generated}} \qquad (5.6)$$

where $N_{mode}^{generated}$ means the generated number of decays in MC for the particular *mode*, and $N_{mode}^{accepted}$ is the number of accepted events for that mode after all selection cuts.

Evidently, the uncertainty in the acceptance comes from a Poisson error in the number of accepted events, while the number of MC generated decays is exact.

The ratio of the acceptances from MC and the observed $2\pi^0$ events from data together contributes a percentage error to N_S via the second term on the right in (5.4).

The last term in (5.4) also contributes a percentage error to N_S. It is simply the percentage error for $\mathcal{B}(K_L \to 2\pi^0)$, or:

$$\frac{0.04 \times 10^{-4}}{8.69 \times 10^{-4}} = 0.46\% \qquad (5.7)$$

Summary of systematic errors

The systematic errors and their magnitudes in terms of ΔN_S are listed below, compared to the fitted N_S and single event sensitivity:

	$X_{181.7}$	$X_{198.0}$	$X_{214.3}$	$X_{230.6}$
fitted N_S	1.02	4.32	-0.51	-6.42
S.E.S.	1.42×10^{-7}	1.04×10^{-7}	1.20×10^{-7}	2.44×10^{-7}
$2\pi^0$ background	0.00	0.02	0.04	0.03
$3\pi^0$ background shape	5.81	0.09	2.98	1.05
$3\pi^0$ background scale	2.97	4.40	3.62	1.88
$\pi^0\gamma\gamma$ background	0.06	0.02	0.09	0.04
mass resolution	0.09	0.07	0.14	0.06
S.E.S./$\mathcal{B}(K_L \to 2\pi^0)$	2.54%	2.17%	2.33%	3.18%
$\mathcal{B}(K_L \to 2\pi^0)$ (PDG)	0.46%	0.46%	0.46%	0.46%

Unsurprisingly, the largest errors come from uncertainties in modelling the $K_L \to 3\pi^0$ background, due to its dominance and low statistics.

5.2.2   Implementation of systematic errors

Systematic errors are implemented into the likelihood function $\mathcal{L}(N_S)$ by means of smearing with a Gaussian function, whose σ is calculated from the systematic errors. Mathematically, it is a convolution:

$$
\begin{aligned}
\mathcal{L}_{smeared}(x) &= \mathcal{L}(x) \otimes G(x; \sigma(x)) \\
&= \int \mathcal{L}(u) \times \frac{1}{\sqrt{2\pi}\sigma(u)} e^{-(x-u)^2/2\sigma^2(u)} du
\end{aligned}
$$

where $\sigma(x)$ is a function of the smearing Gaussian's *mean*:

$$
\sigma(x) = \sqrt{\sum \sigma_\Delta^2 + \sum (\sigma_\% \times x)^2} \tag{5.8}
$$

The systematic errors come in the the form of σ_Δ's and $\sigma_\%$'s in (5.8), where σ_Δ's are the errors in background which do not vary with N_S, and $\sigma_\%$'s are mass resolution and S.E.S. percentage errors that vary with N_S. All errors are summed in quadrature due to the fact they're uncorrelated.

The likelihood function is plotted in Fig. 5.7. The narrower and taller curve represents the original likelihood function, while the smeared likelihood function is overlaid as the wider and lower curve. It also more closely resembles a Gaussian distribution.

5.2.3   Final fitting results

The smeared likelihood function is used to determine an upper limit according to (5.3), and is plotted in Fig. 5.8 along with integration limits (blue=lower,
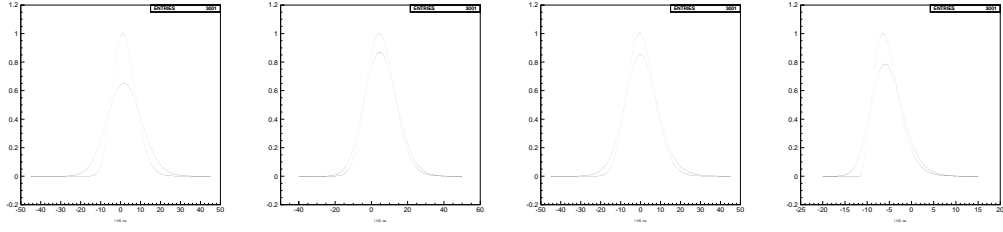
Figure 5.7: Likelihood functions
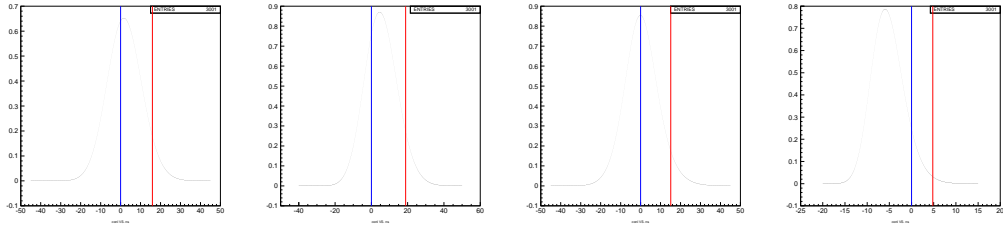
Figure 5.8: Upper limits (blue: $N_S = 0$, red: upper limit on N_S)
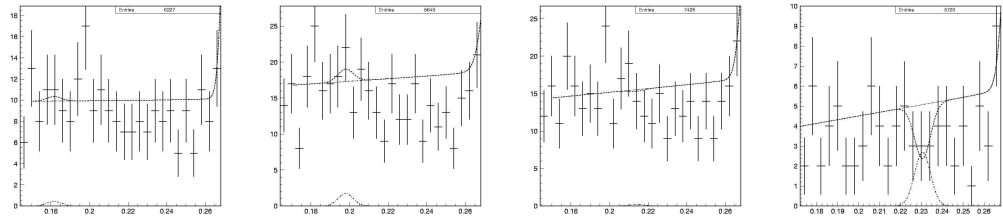
Figure 5.9: Extracted signals ($m_{\gamma\gamma}$, GeV)

$N_S = 0$; red=upper, 90% area). The slightly shifted central value is taken to be the extracted number of signal as shown in Fig. 5.9.

The final result is summarized below:

	$X_{181.7}$	$X_{198.0}$	$X_{214.3}$	$X_{230.6}$
central N_S	1.62	4.58	-0.09	-5.95
$N_S <$	15.93	18.89	15.12	4.78
S.E.S.	1.416×10^{-7}	1.042×10^{-7}	1.199×10^{-7}	2.44×10^{-7}
$\mathcal{B}(K_L \to \pi^0 X) <$	2.26×10^{-6}	1.97×10^{-6}	1.81×10^{-6}	1.17×10^{-6}

5.3 Counting Method

As a verification for the preceding analysis, a straightforward counting method is employed for signal extraction. It is expected that this method should give worse background estimation, due to considering background events in the signal box only but not sidebands. Signal identification is expected to be worse as well because the signal shape is not considered in signal extraction.

Background is estimated by counting the number of events falling inside the signal box from all three MC modes, where the counts follow the Poisson distribution. The independent counts are scaled to the normalization mode of $K_L \to 2\pi^0$ to be combined according to Eqn. (3.5), and error propagated. The combined total background from MC is then further scaled to the data statistics via the normalization mode as described in section 5.1.3.

All numbers used are listed as follows:

	$X_{181.7}$	$X_{198.0}$	$X_{214.3}$	$X_{230.6}$
$2\pi^0$ #/scaled	0/0	0/0	0/0	0/0
$3\pi^0$ #/scaled	7/315.12	19/855.33	15/645.26	6/270.10
$\pi^0\gamma\gamma$ #/scaled	29/1.3282	27/1.2366	39/1.7862	13/0.5954
N_{MC}^{total}	316.45±119.13	856.57±196.36	677.05±174.48	270.70±110.29
$N_{2\pi^0}^{data}/N_{2\pi^0}^{MC}$	5599.7/58747	7607.8/82590	6426.6/69165	4163.7/44448
$N_{data}^{expected}$	30.16±11.37	78.90±18.12	62.91±16.24	25.36±10.34
$N_{data}^{observed}$	39	77	59	11

Similar to the fitting results, the counting method finds no significant physical signal, therefore an upper limit to the branching ratio is estimated.

The upper limit is calculated using the software package POLE++, which is short for "POissonian Limit Estimator, C++ version" [22]. It is developed to "calculate confidence intervals for a Poissonian with background using a frequentist confidence belt construction, with Bayesian treatment of systematic uncertainties" [23][24].

POLE++ takes as inputs:

- the number of observed events
- the expected background and its uncertainty
- signal efficiency and its uncertainty

and outputs a confidence interval according to the user defined confidence level. In addition, the distribution of background uncertainty is set to be Gaussian.

The 90% confidence level results are shown as follows:

	$X_{181.7}$	$X_{198.0}$	$X_{214.3}$	$X_{230.6}$
$N_S <$	33.23	31.5	26.2	7.28
$\mathcal{B}(K_L \to \pi^0 X) <$	4.70×10^{-6}	3.28×10^{-6}	3.14×10^{-6}	1.78×10^{-6}

5.4 K_L Flux

The corrected number of $2\pi^0$ events in data as given in section 5.1.3 allow for estimation of the total K_L flux for Run2:

$$
\begin{aligned}
flux &= \frac{N_{2\pi^0}^{data}/A_{2\pi^0}^{MC}}{\mathcal{B}(K_L \to 2\pi^0)} \\
&= (6426.6 \pm 88.2 \times \frac{69165 \pm \sqrt{69165}}{2 \times 10^9})/(8.69 \pm 0.04) \times 10^{-4} \\
&= 2.14 \times 10^{11} \pm 1.37\%_{stat} \pm 0.38\%_{syst} \pm 0.46\%_{\mathcal{B}(K_L \to 2\pi^0)}
\end{aligned}
$$

Additionally, there are systematic errors from selection cuts, which may arise from differences in data and MC. These errors are considered by comparing each cut's "exclusive" acceptances between data and MC. The exclusive acceptance of a cut is the acceptance of that single cut, calculated when all other cuts are already applied. The differences between data and MC are cast in the form of fractional differences, $F_i = \frac{A_{data,i} - A_{MC,i}}{A_{data,i}}$ for the ith cut.

The systematic error is then calculated as the average of fractional dif-

ferences weighted by inverse acceptance squared [19]:

$$Syst.Err.^2 = \frac{\sum_{i=Allcuts}(F_i/A_{data,i})^2}{\sum_{i=Allcuts}(1/A_{data,i})^2}$$

Details on acceptances for all cuts are listed below:

	run2	2pi0	3pi0	pi0gg	total MC	F^2	1/A^2
cc00	1.000	0.999	1.000	1.000	0.999	0.0000	1.0009
cc02	0.967	0.996	0.224	1.000	0.968	0.0000	1.0684
cc03	0.970	0.991	0.929	1.000	0.991	0.0004	1.0620
cc04sc	0.950	0.948	0.929	1.000	0.948	0.0000	1.1070
cc04cl	0.923	0.888	0.867	0.800	0.888	0.0014	1.1732
cc05sc	0.996	0.991	1.000	1.000	0.991	0.0000	1.0090
cc05cl	0.997	0.991	1.000	1.000	0.991	0.0000	1.0056
cc06	0.992	0.985	0.929	1.000	0.984	0.0001	1.0158
cc07	0.993	0.991	1.000	0.923	0.991	0.0000	1.0149
fb	0.998	0.972	1.000	0.923	0.973	0.0007	1.0031
imb	0.959	0.958	0.382	0.923	0.946	0.0002	1.0880
omb	0.980	0.983	0.929	0.857	0.983	0.0000	1.0411
csiveto	0.603	0.551	0.406	0.545	0.549	0.0082	2.7462
sand	0.997	0.999	1.000	1.000	0.999	0.0000	1.0056
ba	0.952	0.994	0.684	1.000	0.990	0.0016	1.1028
icv	0.999	0.994	0.929	1.000	0.993	0.0000	1.0015
ocv	0.823	0.902	0.765	0.800	0.900	0.0087	1.4749
bhcv	0.998	0.998	1.000	1.000	0.998	0.0000	1.0040
bcv	0.869	0.839	0.722	0.857	0.838	0.0013	1.3249
klz	0.391	0.384	0.096	0.375	0.375	0.0017	6.5486
klpt	0.973	0.964	1.000	0.857	0.964	0.0001	1.0560
klrc6^2	0.933	0.891	0.813	0.923	0.890	0.0021	1.1483
chisq1	0.948	0.967	0.433	0.857	0.957	0.0001	1.1116
chisq3	0.596	0.594	0.565	0.164	0.594	0.0000	2.8198
gamrms1	0.942	0.940	0.342	1.000	0.926	0.0003	1.1279
gamrms2	0.930	0.918	0.464	1.000	0.910	0.0005	1.1556
gamrms3	0.989	0.989	0.929	1.000	0.988	0.0000	1.0230

According to this method, the systematic error from selection cuts is calculated to be 3.85%.

For ease of comparison with the E391a flagship mode, $K_L \rightarrow \pi^0 \nu \bar{\nu}$, we "normalize" the flux number of K_L at collimator 6 to the number of decays in the fiducial region of $340cm < z - vertex < 500cm$. The normalizing factor can be mathematically fixed by the K_L life time and momentum distribution as it leaves collimator 6. In practice, however, this factor is obtained by a special MC sample where generated K_L's are tagged whenever one decays in the fiducial region. For a total of 500k K_L's generated, 11296 were tagged as decayed in the fiducial region. The decay probability, or normalizing factor, is then $(2.2592 \pm 0.0213)\%$.

The flux after normalization is:

$$4.83 \times 10^9 \pm 1.37\%_{stat} \pm 3.87\%_{syst} \pm 0.46\%_{\mathcal{B}(K_L \rightarrow 2\pi^0)} \pm 0.94\%_{normalization} \quad (5.9)$$

or with errors combined:

$$flux = (4.83 \pm 0.21) \times 10^9 \qquad (5.10)$$

Chapter 6

Conclusions and Prospects

6.1 Conclusions

We searched for the hypothetical decay mode, $K_L \to \pi^0 X (X \to \gamma\gamma)$, where the X is the light pseudoscalar sgoldstino with $m_X = 214.3 MeV$. Higher and lower masses were also searched. We've found no significant excess in signal. Upper limits at 90% confidence level were set using a likelihood fitting method:

<div align="center">

Final Result

	$X_{181.7}$	$X_{198.0}$	$X_{214.3}$	$X_{230.6}$
$\mathcal{B}(K_L \to \pi^0 X) <$	2.26×10^{-6}	1.97×10^{-6}	1.81×10^{-6}	1.17×10^{-6}

</div>

This result is checked by a separate signal extraction using the counting method. It is plotted against the result obtained from the fitting method in Fig. 6.1, where the upper limits set by the counting method are consistently higher than those obtained from fitting, just as expected. Their trend versus the target m_X is also consistent between the two methods. This shows that there is no bias in the modelling for the fitting method, and its overall lower upper limits are indeed reliable.

We also estimated the total K_L flux for the E391a Run2 data set. This value directly influences the flagship mode, $K_L \to \pi^0 \nu\bar{\nu}$, and is pursued by a dedicated multi-mode research. This analysis provides another estimate for the $K_L \to 2\pi^0$ mode using different methods as a check. The flux estimates are listed in Table 6.1.
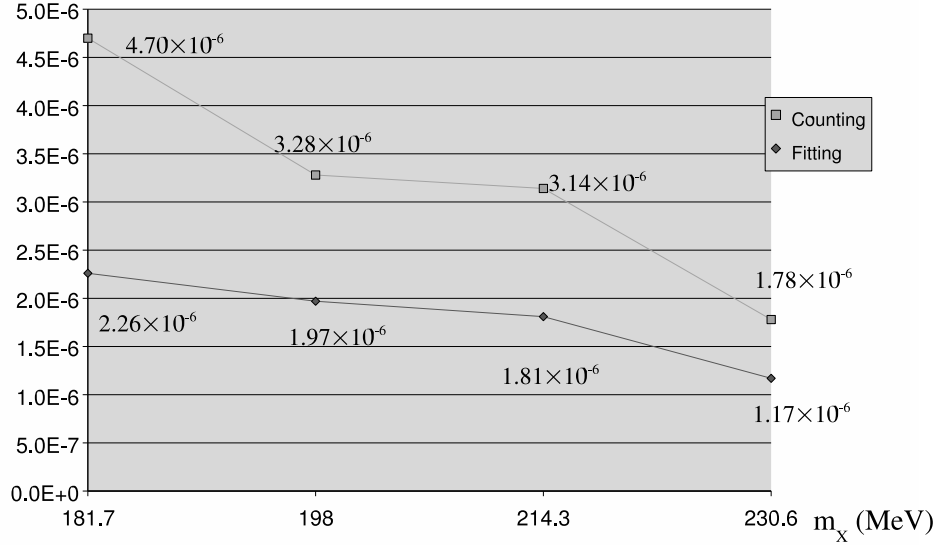
Figure 6.1: Counting vs Fitting

The flux number obtained in this analysis, although lower than the multi-mode research in the $K_L \to \pi^0 \nu \bar{\nu}$ analysis, is well within error for the same decay mode of $K_L \to 2\pi^0$ and is considered consistent.

6.2   Prospects

From the experience gathered in this analysis, we can highlight three possible areas for improvement. They are the increase in data statistics, the increase in Monte Carlo sample statistics and the decrease in size for the CsI crystals in the Electromagnetic Calorimeter. The extent of improvement is roughly estimated.

6.2.1   Increased data statistics – Run3 data set

The Run3 data set is about 87% of the Run2 data set in statistics. The improvement in the upper limit is estimated by scaling both expected background and background uncertainty up by 187%. Observed number of events

Table 6.1: Flux Comparison

mode	flux
$K_L \to 2\pi^0$ (this analysis)	$(4.83 \pm 0.21) \times 10^9$
$K_L \to \pi^0 \gamma\gamma$	$(5.41 \pm 0.37) \times 10^9$
$K_L \to 2\pi^0$	$(5.13 \pm 0.40) \times 10^9$
$K_L \to 3\pi^0$	$(5.02 \pm 0.35) \times 10^9$
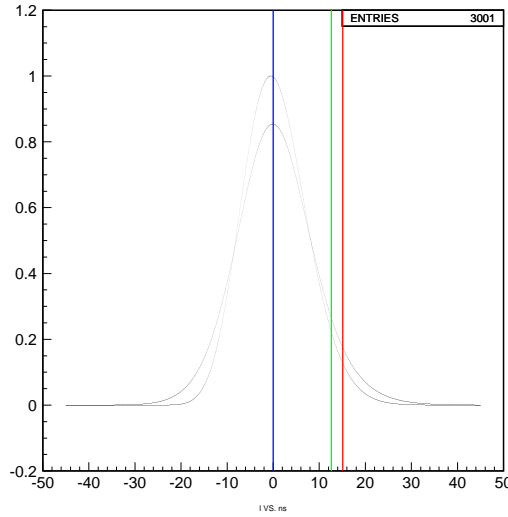
Figure 6.2: Upper limit using the un-smeared likelihood function (red: smeared limit, green: un-smeared limit, blue: $N_S = 0$)

is taken to equal the expected background for the case of no observed signal. These numbers are fed into POLE++, and a 3% decrease in upper limit is estimated.

6.2.2 Increased MC statistics

The dominant source of systematic error in this analysis comes from modelling the $K_L \to 3\pi^0$ background, as shown in section 5.2.1. The possible improvement brought by MC statistics, that's much higher than the current $1/4$ of data equivalent, is estimated using the original un-smeared likelihood function. The CL90 upper limit obtained is found to be 17% lower than using the smeared likelihood function, as shown in Fig. 6.2.

Table 6.2: $3\pi^0$ background fusion categories

N_{CLS}	ngcsi	out of 43(%)	category
4	4	1(2.3%)	2 missing photons
4	5	21(48.8%)	1 missing, single fusion
4	6	21(48.8%)	double fusion

6.2.3 Finer CsI crystals – E14 experiment

As discussed in section 4.4.3, the cluster RMS cut is effective at removing single and double fusion $3\pi^0$ decays. However, due to the large cross section of the CsI crystals, it is difficult to further suppress these fusion events, and they remain the dominant background.

Taken from the $3\pi^0$ MC, Fig. 6.3 shows the *real* number of gamma hits on the CsI (ngcsi), where the events were classified as $N_{CLS} = 4$, have passed through all selection cuts and were found in the (four combined) signal boxes as background events. The composition is listed in Table 6.2.

The E14 experiment will succeed the E391a experiment in the search for $K_L \rightarrow \pi^0 \nu \bar{\nu}$. Its improvements include employing finer CsI crystals (2.5cm×2.5cm instead of the current 7cm×7cm) that should aid in cluster separation: Assuming the minimum incident separation that can be identified as a non-local cluster, R_{min}, to be just the crystal edge length. The fusion probability is then proportional to πR_{min}^2 as shown in Fig. 6.4.

It follows that the fusion probability with E14 crystals compared to that with E391a crystals is only $\frac{\pi \times 2.5^2}{\pi \times 7^2} \simeq 13\%$. This should reduce single fusion by 87% and double fusion by $1 - (13\%)^2 \simeq 100\%$. Referring to Table 6.2, total $3\pi^0$ background will be reduced by 91%. Significance $N_S/\sqrt{N_S + N_B}$ should increase by 3.3 times due to its N_B dominated denominator.

However, this crude model may be over-optimistic about the improvements, considering that the Molière radius of the CsI is 3.8cm. There's also the effect of improved cluster recognition beyond what we have in the cluster RMS. The better estimation should come from a proper MC simulation.
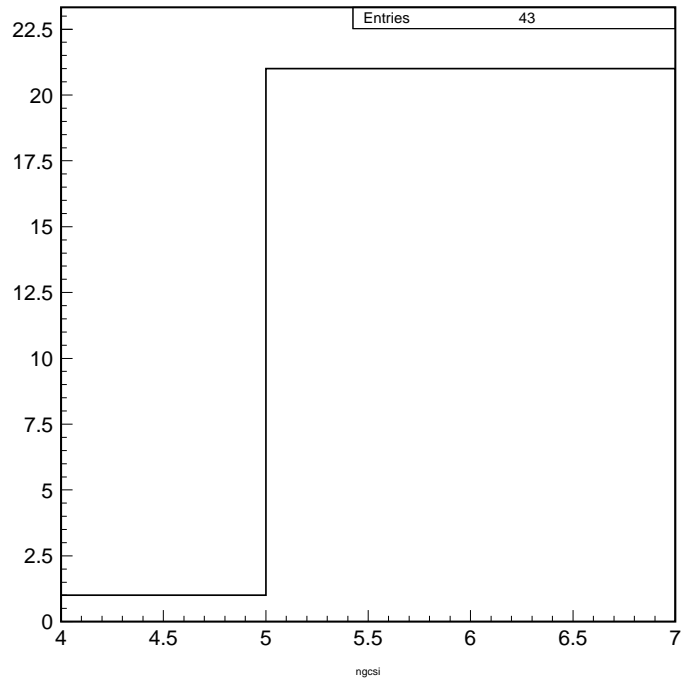
Figure 6.3: Fusion ratio
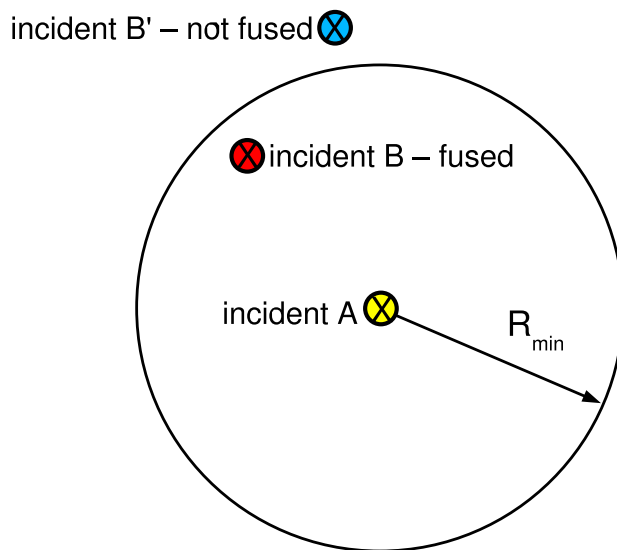
Figure 6.4: Two incidents are fused if $separation < R_{min}$

85

Bibliography

[1] **HyperCP** Collaboration, H. Park *et al.*, "Evidence for the decay Sigma+ → p mu+ mu-," *Phys. Rev. Lett.* **94** (2005) 021801, hep-ex/0501014.

[2] D. S. Gorbunov and V. A. Rubakov, "On sgoldstino interpretation of HyperCP events," *Phys. Rev.* **D73** (2006) 035002, hep-ph/0509147.

[3] D. S. Gorbunov, "Light sgoldstino: Precision measurements versus collider searches," *Nucl. Phys.* **B602** (2001) 213–237, hep-ph/0007325.

[4] D. S. Gorbunov and V. A. Rubakov, "Kaon physics with light sgoldstinos and parity conservation," *Phys. Rev.* **D64** (2001) 054008, hep-ph/0012033.

[5] X.-G. He, J. Tandean, and G. Valencia, "Has HyperCP observed a light Higgs boson?," *Phys. Rev. Lett.* **98** (2007) 081802, hep-ph/0610362.

[6] **KTeV** Collaboration, A. Alavi-Harati *et al.*, "Measurement of the decay K(L) → pi0 gamma gamma," *Phys. Rev. Lett.* **83** (1999) 917–921, hep-ex/9902029.

[7] **NA48** Collaboration, A. Lai *et al.*, "Precise measurement of the decay K(L)→ pi0 gamma gamma," *Phys. Lett.* **B536** (2002) 229–240, hep-ex/0205010.

[8] **Particle Data Group** Collaboration, W. M. Yao *et al.*, "Review of particle physics," *J. Phys.* **G33** (2006) 1–1232.

[9] T. Inagaki *et al.*, "Measurement of the $K_L^0 \to \pi^0 \nu \bar{\nu}$," *Proposal* **TN001** (1996).

BIBLIOGRAPHY

[10] H. Watanabe *et al.*, "Neutral beam line to study K(L)0 → pi0 nu anti-nu decay at the KEK 12-GeV proton synchrotron," *Nucl. Instrum. Meth.* **A545** (2005) 542–553.

[11] M. Doroshenko *et al.*, "Undoped-CsI calorimeter for the K(L)0 → pi0 nu anti-nu experiment at KEK-PS," *Nucl. Instrum. Meth.* **A545** (2005) 278–295.

[12] M. Doroshenko, "Calibration of E391a detector,". TN171.

[13] K. Sakashita, *Search for the decay $K_L \to \pi^0 \nu \bar{\nu}$*. PhD thesis, 2006.

[14] S. Ajimura *et al.*, "Measurement of the photon detection inefficiency of electromagnetic calorimeters at energies below 1-GeV," *Nucl. Instrum. Meth.* **A552** (2005) 263–275.

[15] Y. Akune, "Performance of the Main Barrel," Master's thesis, 2004.

[16] H. Watanabe. PhD thesis, 2002.

[17] M. Yamaga, "DAQ system at the Engineering Run on 2002 for KEK-PS E391a experiment, etc,". TN148.

[18] C. A. S. Group, "GEANT-Detector Description and Simulation Tool," *CERN* **W5013** (1993).

[19] G. Perdue, "MC Tuning and Six Cluster Events,". Technote Draft.

[20] G. D'Ambrosio and J. Portoles, "Vector meson exchange contributions to K → pi gamma gamma and K(L) → gamma l+ l-," *Nucl. Phys.* **B492** (1997) 417–454, hep-ph/9610244.

[21] H. S. Lee, "CsI Angle and Energy correction," *Meeting slides* (Aug, 2005).

[22] J. Conrad, O. Botner, A. Hallgren, and C. Perez de los Heros, "Including systematic uncertainties in confidence interval construction for Poisson statistics," *Phys. Rev.* **D67** (2003) 012002, hep-ex/0202013.

[23] G. J. Feldman and R. D. Cousins, "A Unified approach to the classical statistical analysis of small signals," *Phys. Rev.* **D57** (1998) 3873–3889, physics/9711021.

[24] F. Tegenfeldt and J. Conrad, "On Bayesian treatment of systematic uncertainties in confidence interval calculations," *Nucl. Instrum. Meth.* **A539** (2005) 407–413, physics/0408039.

[25] P. Avery, "Fitting Theory I – V." http://www.phys.ufl.edu/∼avery/fitting.html.

[26] K.-F. Chen, *Measurements of CP-violating Asymmetries and Polarization in b → s Transitions at Belle.* PhD thesis, National Taiwan University, 2005.

Appendix A

$K_L \rightarrow \pi^0 \gamma\gamma$ Monte Carlo

As mentioned in the introduction, the decay $K_L \rightarrow \pi^0\gamma\gamma$ has been measured by both the KTeV experiment at Fermilab [6] and with the NA48 detector at CERN SPS [7], following the theoretical work of D'Ambrosio and Portolés [20].

The theory is developed in the framework of Chiral Perturbation Theory (χPT), including $\mathcal{O}(p^6)$ corrections and vector meson exchange contributions. An effective coupling constant a_V parametrizes the vector meson exchange contributions, affecting both the branching ratio of $K_L \rightarrow \pi^0\gamma\gamma$ and the decay Dalitz variables z and y, where

$$
\begin{aligned}
z &= (m_{34}/m_K)^2 \\
y &= |E_3 - E_4|/m_K
\end{aligned}
$$

with E_3, E_4 being the energies of the non-π^0 photons in the kaon center of mass frame and m_{34} their invariant mass.

For the Monte Carlo generation, we use the numeric routine from D'Ambrosio and Portolés to generate the z distribution with $a_V = -0.54$[8]. For each event, the value of z is obtained by a standard 2D random number scan on the z probability distribution as shown in Fig. A.1. The z value is then converted to m_{34} and used as the mass of the "intermediate state" for the non-π^0 photons.

The decay generation is verified also with the help of the D'Ambrosio and Portolés routine, which outputs the y distribution corresponding to the z distribution. Immediately following their decay from the "intermediate state", the photons are boosted back to the K_L rest frame to have their y
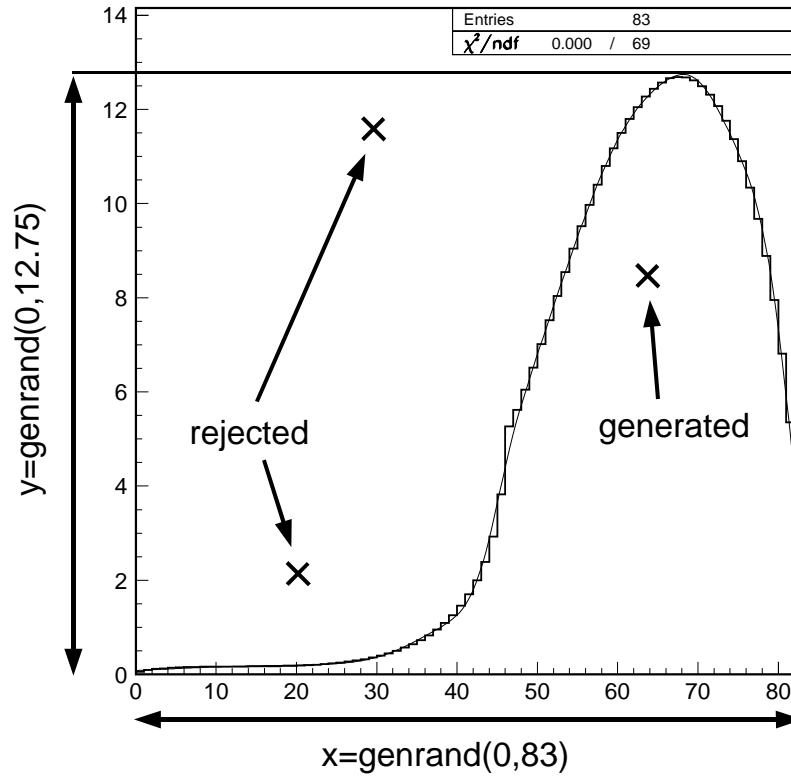
Figure A.1: The z distribution and the random number scan (x axis to be normalized: [0:83]→[0:0.53])
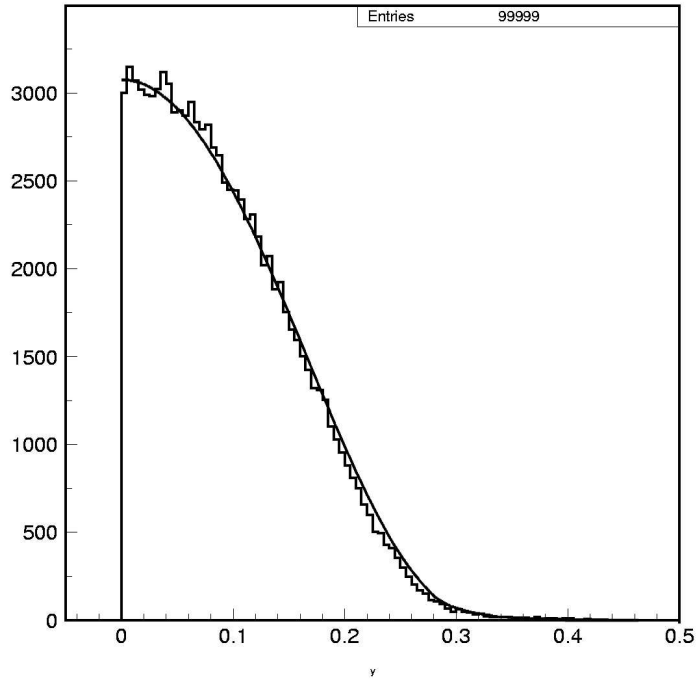
Figure A.2: Overlay of variable $y = |E_3 - E_4|/M_K$ (line: calculated, histogram: generated MC)

value stored. It is plotted against the separately calculated y distibution in Fig. A.2.

Finally, the generated $K_L \to \pi^0 \gamma\gamma$ decays are combined with other modes according to its PDG branching ratio, as discussed in section 3.6.

Appendix B

Kinematic Fitting

The kinematic fitting method [25][26] combined with suitable constraints benefits us by a) providing a χ^2 value which indicates the probability that our hypothesis (i.e. this event is a $K_L \to \pi^0 + something$ decay) is correct, and b) improving measured and unknown variables which also satisfy the constraint conditions (i.e. improving $m_{\gamma\gamma}$ resolution).

The fitting variables (12) are the positions and energies of the 4 incident photons, and the unknown variables (3) are the calculated decay vertex:

$$\alpha = \left(x_{\gamma_1}, y_{\gamma_1}, E_{\gamma_1}, x_{\gamma_2}, ..., x_{\gamma_4}, y_{\gamma_4}, E_{\gamma_4} \right) \tag{B.1}$$

$$v = \left(v_x, v_y, v_z \right) \tag{B.2}$$

where $\gamma_{1,2}$ are decayed from the π^0 and $\gamma_{3,4}$ from the X. The equation of constraint would then be written as:

$$H(\alpha, v) = 0 \tag{B.3}$$

where H is a vector with as many components as constraints. In this case it would be:

$$H_1 = \left(E_{\gamma_1} + E_{\gamma_2} \right)^2 - \left(\mathbf{p}_{\gamma_1} + \mathbf{p}_{\gamma_2} \right)^2 - m_{\pi^0}^2$$

$$H_2 = E_{K_L}^2 - \mathbf{p_{K_L}}^2 - m_{K_L}^2$$

$$H_3 = \sum_i E_{\gamma_i} x_{\gamma_i} - E_{K_L} v_x \frac{z_{CsI} - z_{target}}{v_z - z_{target}}$$

$$H_4 = \sum_i E_{\gamma_i} y_{\gamma_i} - E_{K_L} v_y \frac{z_{CsI} - z_{target}}{v_z - z_{target}}$$

An expansion for H around the point α_A and v_A gives:

$$H(\alpha, v) = H(\alpha_A, v_A) + \left[\frac{\partial H}{\partial \alpha}\right]_{\alpha_A} (\alpha - \alpha_A) + \left[\frac{\partial H}{\partial v}\right]_{v_A} (v - v_A) = 0 \quad \text{(B.4)}$$

or in matrix notation:

$$d + D(\alpha - \alpha_A) + E(v - v_A) = 0 \quad \text{(B.5)}$$

with the matrices D and E called the "core matrices", given by differentiations on H with respect to α and v.

The Lagrangian multipliers approach is applied in iterations, defining first:

$$V_D = (DV_{\alpha_0}D^T)^{-1} \quad \text{(B.6)}$$
$$V_E = (E^T V_D E)^{-1} \quad \text{(B.7)}$$

where V_{α_0} is the error matrix evaluated at the original measured values, α_0. Then, in each iteration, the Lagrangian multipliers and χ^2 are evaluated:

$$\lambda_0 = V_D[D(\alpha_0 - \alpha_A) + d] \quad \text{(B.8)}$$
$$\chi^2 = \lambda_0^T[D(\alpha_0 - \alpha_A) + E(v_0 - v_A) + d] \quad \text{(B.9)}$$
$$\lambda = \lambda_0 - V_D E V_E E^T \lambda_0 \quad \text{(B.10)}$$

With their help, updated fitted measurements and updated unknown variables are obtained:

$$\alpha = \alpha_A - V_{\alpha_0}D^T\lambda \quad \text{(B.11)}$$
$$v = v_A - V_E E^T \lambda_0 \quad \text{(B.12)}$$

In each following iteration, the core matrices are re-evaluated at the new α_A and v_A, followed by updating λ_0, χ^2 and λ. Finally the vectors α and v are updated again for the next iteration. To minimize χ^2, it is compared with that from the previous iteration. If it is found smaller, the loop continues; if it is found larger, the loop is terminated and α and v from the previous iteration are used.

Degrees of freedom

The fit applied here has 3 unknowns calculated under 4 constraints as mentioned earlier. This leaves the fit with $4 - 3 = 1$ degree of freedom.